

SIPM ARRAYS AS READOUTS FOR THE GLUEX BARREL CALORIMETER

A Thesis
Submitted to the Faculty of Graduate Studies and Research
In Partial Fulfillment of the Requirements
for the Degree of
Master of Science
In
Physics
University of Regina

by
Shaun Thomas Krueger
Regina, Saskatchewan
May, 2014

Copyright 2014: S. Krueger

Abstract

The GlueX experiment at Jefferson Lab seeks to map out gluonic degrees of freedom in order to gain a better understanding of gluons and their interactions with quarks towards elucidating the phenomenon of confinement in Quantum Chromodynamics. In order to accomplish this goal the experiment must be able to detect and measure the four-momentum of a large percentage of the photons produced. A key component in the study of these photons will be the Barrel Calorimeter (BCAL).

As a critical component of the GlueX experiment, the BCAL must be fully tested and operational before the beam is delivered to Hall D, the newest experimental Hall at Jefferson Lab. In order to ensure the integrity of the optical light guides attached to the face of every module, cosmic muon tests and LED pulser measurements were conducted to test the uniformity of light transmission. It was found that the modules behaved as expected and that the LED monitoring system was operational.

Acknowledgments

I would like to thank Dr. Papandreou for his assistance, both financially and academically throughout my period as a graduate student.

I would also like to thank Dr. Elton Smith and the many other wonderful people at Jefferson Labs for the help they have given me on my trips there as well as his guidance and support for my experiment.

The assistance Dr. Semenov provided in programming was invaluable as well as the many useful insights into data analysis.

Lastly I would like to thank Dr. Lolos for the time and effort he dedicated to editing my thesis.

Dedication

To the love of my life, Josie, thank you for your compassion, support, and patience.

Contents

List of Figures	ix
List of Tables	x
Nomenclature	xi
1 Introduction	1
1.1 Outline of thesis	3
2 Theoretical Motivation	5
2.1 The Standard Model	5
2.2 Quantum Chromodynamics	7
2.3 Hadronic Physics	9
2.4 Exotics - Glueballs and Hybrid Mesons	12
2.5 Hybrid Meson Production	13
2.6 Hybrid Meson Detection	15
3 The GlueX detector	17
3.1 Overview	17
3.1.1 Electron Beam	20
3.1.2 Charged Particle Tracking	22

3.1.3	Calorimetry	22
3.1.4	Particle Identification	23
3.2	Barrel Calorimeter	24
3.2.1	Light Guides	28
4	Silicon Photomultipliers	31
4.1	Introduction	31
4.2	Avalanche Photodiode	32
4.3	Silicon Photomultipliers	35
4.3.1	Photon Detection Efficiency	37
4.3.2	Recovery Time	38
4.3.3	Linearity	39
4.3.4	Dynamic Range	40
4.4	SiPM Noise	40
4.4.1	Dark Rate	41
4.4.2	Optical Cross Talk	41
4.4.3	GlueX Specifications	42
5	Readout Assemblies	43
5.1	Introduction	43
5.1.1	Readout Assemblies	43
5.2	SiPM Binning	47
5.2.1	Determining the Resistors	50
6	Module Calibration Tests	54
6.1	Introduction	54
6.2	Experimental Setup	56

6.3	LEDs	57
6.3.1	Monitoring system	57
6.3.2	LED Measurements	61
6.3.3	Results	66
6.4	Cosmic Radiation	67
6.4.1	Preliminary Preparation	67
6.4.2	Energy Determination	71
6.4.3	Timing Information - TDC	73
6.4.4	Timing Information - fADC	76
6.4.5	Sloped Tracks	77
6.5	Results	78
7	Conclusions	90
	Appendices	91
A	Author's Contributions:	92
	References	93

List of Figures

1.1	JLab Accelerator Site	2
2.1	The Standard Model	6
2.2	The Flux Tube Model	8
2.3	The Meson Nonet	10
3.1	GlueX Detector Systems	18
3.2	Beam Line	21
3.3	BCAL Lead Scintillating Fibre Matrix	25
3.4	BCAL Schematic View	26
3.5	Light Guide on BCAL	29
3.6	Light Guide Dimensions	30
4.1	PMT Schematic	32
4.2	P-N Junction and the Depletion Zone	33
4.3	Breakdown of APD	34
4.4	SiPM Pixel	36
4.5	APD versus Wavelength	38
5.1	SiPM Schematic	44
5.2	Readout Assembly	45

5.3	Summation Segmentation	47
5.4	Electronics Circuit	49
5.5	SiPM Voltage Offset	53
6.1	Experimental Setup	57
6.2	SiPM Bias Distribution	58
6.3	LED Components	60
6.4	LED Pulses	64
6.5	LED Reflection	67
6.6	Cosmic Muon Signal	69
6.7	Signal Requirements	70
6.8	Threshold Determination	70
6.9	Integration Window	71
6.10	ADC to MeV Conversion Factor	72
6.11	Consistency of Conversion Factor	73
6.12	Readout schematics	75
6.13	Readout schematics	77
6.14	fADC Timing - Scatter Plot	79
6.15	fADC Timing - Histogram	80
6.16	Muon Path	81
6.17	Muon Path - Histogram	81
6.18	Uncorrected Energy Distribution	82
6.19	Corrected Energy Distribution	82
6.20	Upstream Energy Distribution - All Modules	84
6.21	Up/Down Ratio - Single Module	86
6.22	Up/Down Ratio - All Modules	87

6.23 Readout Cells - Ratio	89
--------------------------------------	----

List of Tables

2.1	Exotic Hybrid Mesons	13
5.1	Resistors	52
5.2	SiPM Spread	52
6.1	LED Power Distribution	63
6.2	Energy Deposition	83
6.3	Readout Cell Ratios	88
6.4	Readout Cell Ratios	88

Nomenclature

ADC Analog to Digital Converter

APD Avalanche Photodiode

BCAL Barrel Calorimeter

CDC Central Drift Chamber

FCAL Forward Calorimeter

LED Light-Emitting Diode

FDC Forward Drift Chamber

MIP Minimum Ionizing Particle

PID Particle Identification

PMT Photo-multiplier Tube

PWA Partial Wave Analysis

QCD Quantum Chromodynamics

QED Quantum Electrodynamics

SiPM Silicon Photomultiplier

SM Standard Model

SQM Simple Quark Model

TDC Time to Digital Converter

TOF Time of Flight

Chapter 1

Introduction

A strong human desire is to understand the Universe and its governing forces. While much of the macroscopic world is well understood, many aspects of the microscopic world remain a mystery. In order to elucidate some of these, the Thomas Jefferson National Accelerator Facility (JLab) was constructed in Newport News, Virginia. Since 1994 research has been conducted in three experimental Halls (A, B, and C) with a 6 GeV electron beam in order to unlock various features of the nuclear force [1]. While significant advancements were accomplished in that time, in August 2009 construction began on the accelerator facility in order to upgrade the beam capabilities to 12 GeV (Figure 1.1) allowing access to a whole new realm of nuclear research. Five new cryomodules were added to the existing 20 that were in place on each linear segment of the accelerator in order to increase the maximum acceleration boost to 2.2 GeV per pass. In order to handle these new upgrades the central helium liquefier plant capacity was increased. Along with these upgrades a new experimental hall, Hall D, was constructed to house the GlueX experiment, named for the search of gluonic excitations as well as a new arc to deliver the beam.

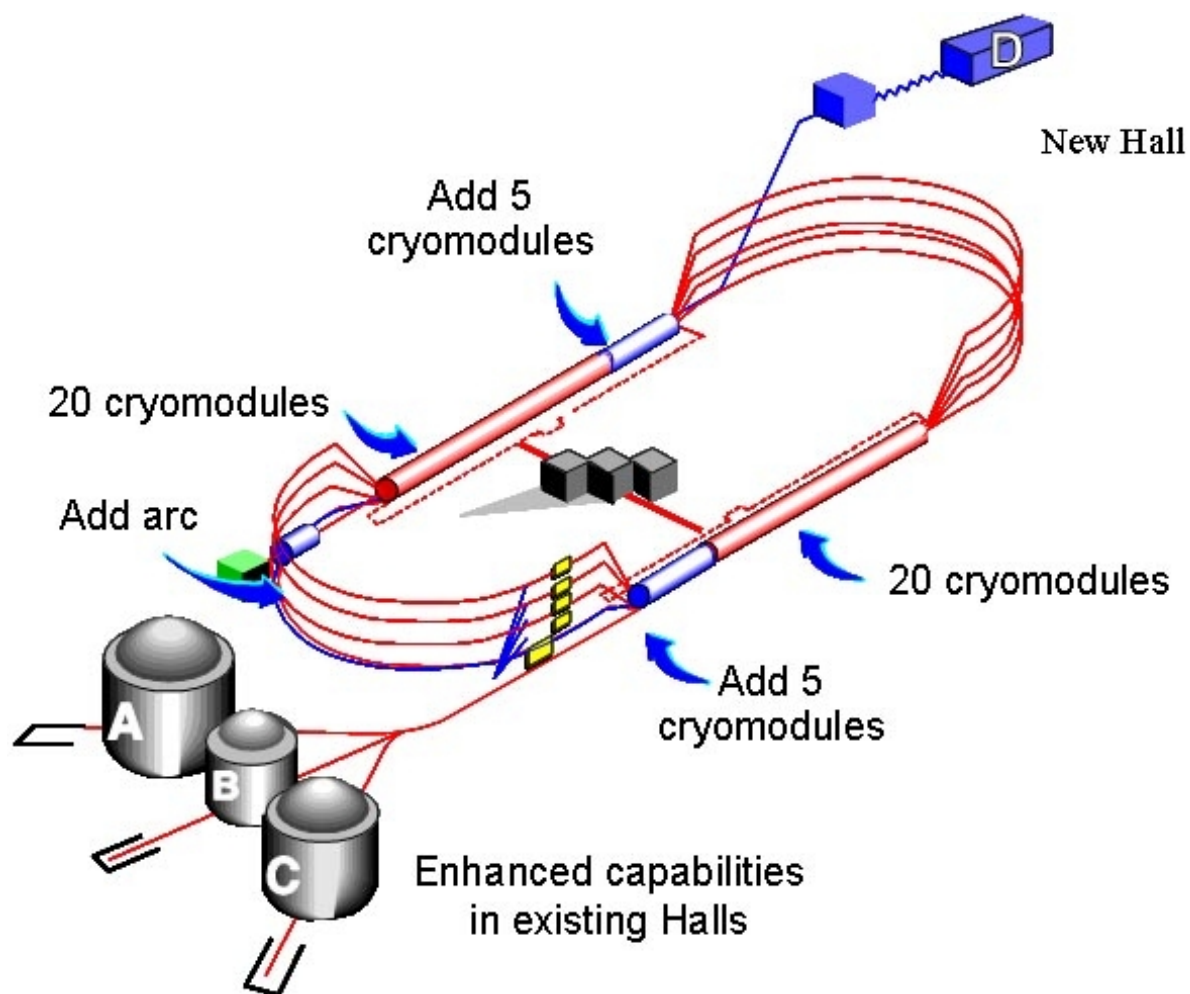


Figure 1.1: Diagram showing the JLab accelerator site including the four experimental Halls as well as the additional cryomodules used to upgrade the beam energy to 12 GeV from the original 6 GeV and a new arc leading to Hall D. Image courtesy of the GlueX Collaboration.

1.1 Outline of thesis

The principles behind Quantum Chromodynamics (QCD) and the Standard Model (SM) are outlined in Chapter 2 as theoretical background. Following this, the nature of exotic hybrid mesons is provided as they will be used to show explicit signatures of gluonic degrees of freedom. While other experiments have established the role of gluons in QCD, it is the hope of GlueX to be able to provide a firm understanding of the nature of gluons and the confinement of quarks and gluons within a particle in the static (low energy) limit.

An experimental overview of the GlueX project is given in Chapter 3, which outlines each component of the GlueX detector and its respective roles in measuring the decay products of hybrid mesons. Special emphasis is placed on the Barrel Calorimeter (BCAL) as it pertains to its readout assemblies. The BCAL, a key detector subsystem of the GlueX experiment, is a nearly hermetic photon detector, constructed from 48 wedge shaped blocks referred to as modules. Each module is equipped with two readout assemblies attached to either end to collect data, each utilizing 40 large area Silicon Photomultiplier (SiPM) arrays. These readout assemblies were designed to offer consistent responses for all units.

In Chapter 4 an explanation of SiPMs is given in order to provide an understanding of their operation and the role they will play in the readout assemblies.

The assemblies themselves are discussed in Chapter 5 with a focus on the arrangement of the 3840 SiPMs used within the 96 readout assemblies and the challenges faced with their implementation.

The tests that were conducted on the modules and their respective light guides are presented in Chapter 6. The light guides were tested through the use of LEDs in order to map out their response for future quality assurance checks that will be done

throughout the lifetime of the experiment. The responses of the modules were also tested through cosmic radiation in order to determine the energy deposition within each module and the uniformity of those results.

The results are summarized in Chapter 7 as well as the effects they will have on the GlueX project and what may occur in the future.

Chapter 2

Theoretical Motivation

2.1 The Standard Model

Every interaction that takes place throughout the Universe is manifested through one of the four fundamental forces of nature: the gravitational, electromagnetic, weak, and strong. One of the main goals of physicists is to derive a general equation that would combine these forces to determine all possible interactions. Working towards that end, the Standard Model (SM) was developed that describes the electromagnetic, weak, and strong forces. According to the SM, all matter is comprised of twelve elementary particles called fermions (and their respective antiparticles), which can be further broken down to six quarks and six leptons as well as four gauge bosons, as shown in Figure 2.1. The six quarks are the up, down, charm, strange, top, and bottom, which carry a fractional electric charge as well as a colour charge of either red, green, or blue. The up, charm, and top quarks carry $+\frac{2}{3}e$ charge while the down, strange, and bottom quarks have $-\frac{1}{3}e$ charge. The antiquarks have all the same properties as their quark counterparts except for having opposite charge, both electric and colour. Opposite colour (anticolour) here means that a colour-anticolour

Quarks	2.4 MeV $\frac{2}{3}$ $\frac{1}{2}$ u up	1.27 GeV $\frac{2}{3}$ $\frac{1}{2}$ c charm	171.2 GeV $\frac{2}{3}$ $\frac{1}{2}$ t top	0 0 1 γ photon
	4.8 MeV $-\frac{1}{3}$ $\frac{1}{2}$ d down	104 MeV $-\frac{1}{3}$ $\frac{1}{2}$ s strange	4.2 GeV $-\frac{1}{3}$ $\frac{1}{2}$ b bottom	0 0 1 g gluon
	<2.2 eV 0 $\frac{1}{2}$ ν_e electron neutrino	<0.17 MeV 0 $\frac{1}{2}$ ν_μ muon neutrino	<15.5 MeV 0 $\frac{1}{2}$ ν_τ tau neutrino	91.2 GeV 0 1 Z^0 weak force
Leptons	0.511 MeV -1 $\frac{1}{2}$ e electron	105.7 MeV -1 $\frac{1}{2}$ μ muon	1.777 GeV -1 $\frac{1}{2}$ τ tau	80.4 GeV ± 1 1 W^\pm weak force
				Bosons (Forces)

Figure 2.1: The Standard Model consists of 16 particles grouped in quarks, leptons, and bosons. Their masses (in MeV or GeV), charge, and spin are also shown.

combination results in a colourless (white) particle. The interactions described by the SM occur through the exchange of gauge bosons which serve as force carriers. The gauge bosons are the photon, mediating the electromagnetic force; the Z^0 , W^+ , and W^- mediating the weak force, and the gluon mediating the strong force.

A theory known as Quantum Chromodynamics (QCD) is used to explain the strong interaction and how gluons interact with quarks. The development of QCD was guided from the success of another quantum field theory, Quantum Electrodynamics (QED). Whereas QCD has similarities to QED there is a key difference, which adds considerable complexity to the former, and is described in the following section.

2.2 Quantum Chromodynamics

QED is a quantum field theory that states that the force between two charged particles, the electromagnetic force, can be expressed as the exchange of a virtual photon, a transient particle that exhibits many characteristics of a photon but does not conserve energy in a nuclear exchange/interaction. QCD works in much the same way as QED, except instead of a virtual photon mediating the force between two charged particles, a gluon is exchanged between two quarks. The added layer of difficulty arises when the colour charge of quarks and gluons is taken into account. In QED there is only a single type of charge that must be dealt with, whereas in QCD there are three different colour charges applied to quarks: green, red, and blue, as well as their respective anticolours. In addition to this, gluons also carry colour charge unlike the photon which is neutral and that gives rise to gluon-gluon interactions.

An interesting property of QCD is that of confinement, which prevents quarks from being isolated from one another. Quarks are bound together by gluons to form hadrons, either in pairs (mesons) or in triplets (baryons). The gluons form a

colour charged flux tube (or string) according to the Flux Tube Model owing to their self interaction (gluon-gluon coupling), as is depicted in Figure 2.2 for a meson [2]. Attempting to separate two quarks by supplying energy will cause the flux tube to stretch. The force of attraction between two quarks remains constant regardless of the distance, since the number of flux lines per unit area in the region between q and \bar{q} remains constant, which in turn leads to a potential that increases linearly with separation distance. As the quarks are pulled apart, more energy will be added to the system until a threshold is reached, where it is more energetically favourable to create a new quark-antiquark pair from the excess energy rather than further stretching the flux tube. Infinite energy is required to separate quarks to infinity, thus making it impossible to isolate a single quark.

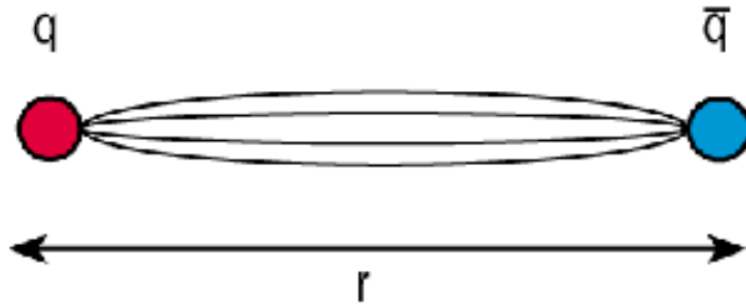


Figure 2.2: The Flux Tube Model states that quarks are bound together by gluons as shown in this sketch where flux cords (or strings) are seen connecting two quarks to form a meson ($q\bar{q}$).

As the distance becomes smaller, another extreme opposite to that of confinement begins to occur. When the distance decreases to a very small range, in the order of 10^{-16} m, quarks and gluons interact only very weakly, a phenomenon known as asymptotic freedom [3]. Such distances are probed at high energies to indirectly detect scattering off individual quarks or gluons and not the entire quark gluon system, a process known as deep inelastic scattering [4].

2.3 Hadronic Physics

Hadrons are broken up into two groups, based on their quark composition: mesons, consisting of a single quark and an antiquark, and baryons, consisting of either three quarks or three antiquarks. The fractional electric charge of each quark within the hadron adds to give each hadron its overall integer charge.

For example, the proton, a hadron comprised of two up quarks and a down quark, will have a +e charge while the neutron, consisting of one up quark and two down quarks is electrically neutral. The colour charge of each quark also adds within the hadron, however, for the case of the colour charge, the net result must always add to white, either by combining a colour and its anticolour, or by combining all three colours (or anticolours).

In order to classify the large number of hadrons that were being discovered, the Simple Quark Model (SQM) was created to classify hadrons based upon their quarks [55]. This classification system is based upon each hadron being composed of a single set of quarks (two for mesons or three for baryons). In reality, hadrons also consist of virtual quarks and gluons; however, these do not affect the SQM properties of the hadron and are largely disregarded in this model. For mesons it is possible to have any one of the three flavours of quarks combined with any of the three flavours of antiquarks, which is expressed mathematically as

$$3 \otimes 3 = 8 \oplus 1 \quad (2.1)$$

where the \otimes and the \oplus represent tensor operations.

This group system of nine particles is referred to as a nonet with the 8 representing the octet while the 1 represents the singlet. The nonet is visually illustrated in Figure 2.3 with the particles organized based on their total charge, Q, and their

strangeness, S . The singlet is unique in that not only are the S and Q values 0 but its isospin, an additional quantum number, is also 0. This representation of quarks is referred to as an $SU(3)$ symmetry group. It should be noted that baryons are categorized in a very similar fashion except that there are three 3 s ($3 \otimes 3 \otimes 3$) to represent the three flavours that each of the three quarks may take on.

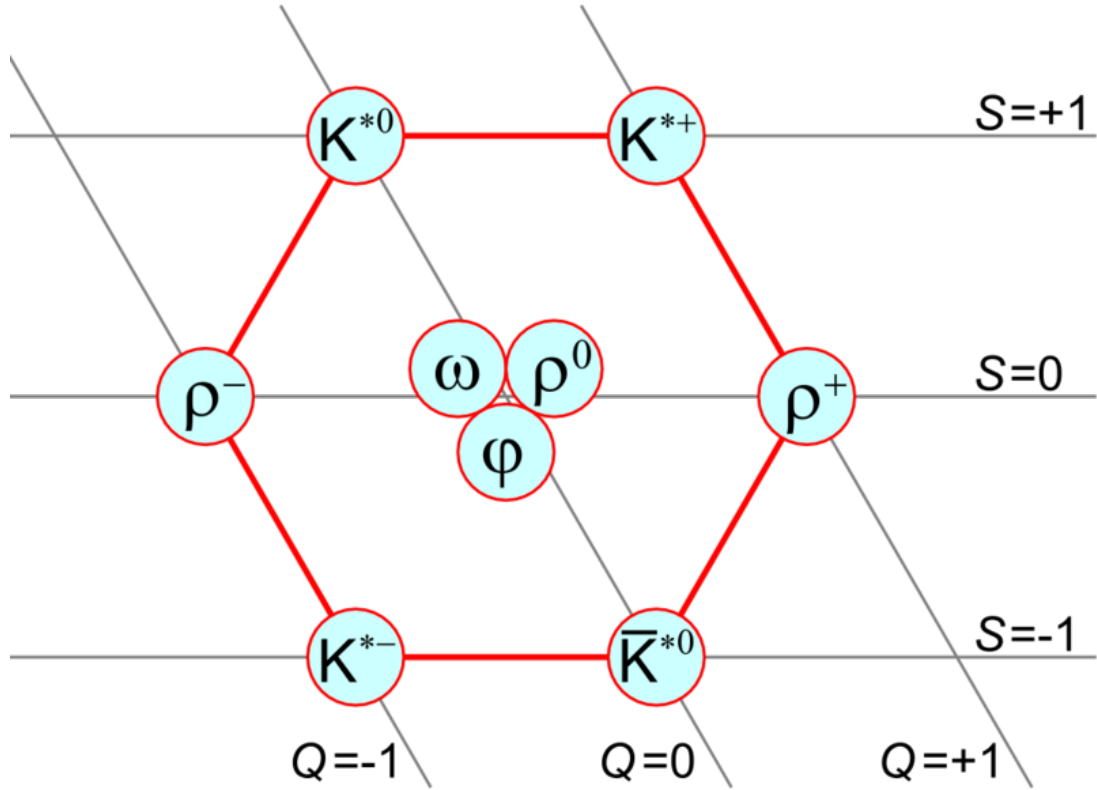


Figure 2.3: The meson vector nonet for J^{PC} equal to 0^{-+} where ϕ is the singlet [6].

The SQM is based on the assumption that matter consists only of the three lightest quarks as they form all stable particles. It is possible however to construct the $SU(6)$ group by replacing the 3 s by 6 s in Equation 2.1 to form all possible combinations of quarks. This form now represents the full extent of QCD.

Each nonet is constructed such that its particles can be characterized by a set of unique quantum numbers, expressed in the form of J^{PC} , where \vec{J} is the total angular

momentum, P is the parity, and C is the charge conjugation. \vec{J} is determined from the total orbital angular momentum, \vec{L} , and the total spin, \vec{S} , of the quarks resulting in \vec{J} being

$$\vec{J} = \vec{L} + \vec{S} \quad (2.2)$$

For mesons, the quark and antiquark pair result in a total spin of $\vec{S} = \vec{S}_1 + \vec{S}_2$, which equals either 0 or 1.

The P and C terms take on either +1 or -1 values representing the state of a system. Parity (P) expresses the symmetry of a system under spatial inversion. The sign of a system can be determined through the equation $P = (-1)^{L+1}$. Charge conjugation (C) is the symmetry of the system arising from the replacement of quarks with their respective antiquarks and vice versa, and is expressed mathematically as $C = (-1)^{L+S}$ for mesons [7].

In the SQM, all contributions to the J^{PC} quantum numbers would come from the quarks resulting in only certain mathematically allowed combinations. For mesons, the spins can either be aligned or antialigned resulting in a spin of 1 or 0 respectively. Considering the cases where L can either be 0 or 1, only six possible states are allowed: 0^{-+} , 0^{++} , 1^{--} , 1^{+-} , 1^{++} , 2^{++} . All other states are forbidden [8].

One of the greatest strengths of the SQM classification system is that it provides the ability to predict the existence of currently undiscovered hadrons in incomplete groupings. The discovery of a single meson will automatically imply the existence of the other eight particles consisting of the same J^{PC} combination. This method was used to numerically determine the mass and lifetime of the Ω^- particle before its discovery and helped experimentalists determine the appropriate energy regime to probe for it [55].

In the end, however, gluons must play a role in hadrons, and to investigate this physics beyond the SQM must be investigated.

2.4 Exotics - Glueballs and Hybrid Mesons

In order to search for explicit gluonic degrees of freedom it is first necessary to utilize particles in which the gluonic signature would be distinct. One method is to search for hadrons comprised entirely of gluons referred to as glueballs [9]. As gluons carry colour charge, they are able to bind to themselves, allowing for glueballs to form. Glueballs should be able to take on any possible combination of J^{PC} , with mass calculated to range from $1.4 \text{ GeV}/c^2$ to nearly $5 \text{ GeV}/c^2$ [10]. Experiments have searched for the lightest of these glueballs but have resulted in only limited success due to the mixing of states that occurs between glueballs and conventional mesons. Mixing is an aspect of quantum mechanics that causes each observed particle to be a linear superposition of all particles that share the same quantum numbers and decay modes. Particles are identified through these quantum numbers and decay modes making it difficult, if not impossible, to state whether an observed particle was a glueball or simply a conventional hadron sharing the same J^{PC} value. To provide explicit evidence of gluons, it is necessary to find a particle exhibiting gluonic excitations that does not share the same J^{PC} values with conventional mesons.

Such particles should exist in the form of hybrid mesons. When determining the J^{PC} values in the SQM it was assumed that the gluons did not contribute to the quantum numbers of the mesons, however, this cannot be true. The Flux Tube Model stipulates that it is possible for the gluonic flux tubes to become excited, thus contributing to the total angular momentum of the system [11]. This allows for the formation of new J^{PC} values, some of which are conventionally forbidden.

Table 2.1 shows the eight expected nonets of hybrid mesons of which three of these states had been previously forbidden. By detecting these forbidden, or exotic, states, it is possible to provide irrefutable proof of gluonic degrees of freedom. One of the primary goals of the GlueX experiment is to completely map out these exotic hybrids, which will require a mass ranging from $1.8 \text{ GeV}/c^2$ to $2.8 \text{ GeV}/c^2$ [12].

Table 2.1: A selection of hybrid mesons and their quantum numbers is tabulated. Note that three J^{PC} combinations are forbidden under the SQM and are thus labeled exotic.

J_g	$S_{q\bar{q}}$	J^{PC}	Type	Sample Members
1	0	1^{++}	normal	a_1, f_1, f'_1
1	0	1^{--}	normal	ρ_1, ω_1, ϕ_1
1	1	0^{-+}	normal	π_0, η_0, η'_0
1	1	0^{+-}	exotic	b_0, h_0, h'_0
1	1	1^{-+}	exotic	π_1, η_1, η'_1
1	1	1^{+-}	normal	b_1, h_1, h'_1
1	1	2^{-+}	normal	π_2, η_2, η'_2
1	1	2^{+-}	exotic	b_2, h_2, h'_2

2.5 Hybrid Meson Production

In order to produce the desired hybrid mesons it is necessary to probe a target nucleon with a particle beam, traditionally done using either pions (π) or kaons (K). The quark and antiquark pair in both the π and K mesons have their spins anti-aligned such that their J^{PC} is 0^{-+} . When an excited flux tube is included for consideration, the possible J^{PC} values are either 1^{++} or 1^{--} , neither of which are exotic. Any attempt to access the exotics through an intermediate spin flip would severely suppress meson production to the extent where the desired signal is indistinguishable from the background generated by all normal channels.

A photon beam, however, will have a J^{PC} value of 1^{--} which, after accounting for

an excited flux tube, will allow for six possible combinations of J^{PC} in which all three exotic cases are included. While photons are unable to undergo hadronic interactions themselves, a photon beam will contain virtual ρ , ω , and ϕ mesons that have the same set of quantum numbers of the γ due to the linear superposition of quantum states [13]. It is these virtual mesons, that will interact with the target nucleus to produce the hybrid mesons which will provide evidence of gluonic excitations.

By using a 9 GeV photon beam on a hydrogen (proton) target, it is possible to map out the entire light quark hybrid meson spectrum. This beam is produced by impinging a 12 GeV electron beam on a 20 μm diamond wafer causing coherent Bremsstrahlung radiation¹. In order to meet this energy demand the Jefferson Lab accelerator facility was upgraded by doubling its energy from 6 GeV to 12 GeV, made possible by improvements to the radiofrequency accelerating sections and other crucial components.

The GlueX experiment was designed towards the production of hybrid mesons. While hybrid baryons are also allowed by QCD rules, they lack the exotic characteristics that will provide the smoking gun of gluonic properties that can be found through hybrid mesons. These hybrid baryons would be expected to appear as an overpopulation of states already populated with conventional baryons (constructed from three quarks alone). Currently, however, the experimental evidence shows that there is an underpopulation of states from models based on conventional baryons, not an overpopulation as would be expected if hybrid baryons existed. There are currently efforts underway at Jefferson Lab to identify what effects may be causing this [14].

¹The emission of a photon when a charged particle is decelerated by another charged particle.

2.6 Hybrid Meson Detection

The interaction between a photon and proton in the GlueX experiment will result in the production of a number of mesons, both normal and hybrid, along with a recoiling proton or neutron. These particles will undergo a series of decays in a very short period of time, resulting in a combination of short and long lived normal mesons. As these initial, exotic decays, decays happen very quickly, it is impossible to directly measure the exotic mesons that had been initially produced and, instead, only the remaining stable and long lived particles from secondary decays can be directly measured. Working with only the initial state (determined from the photon momentum), and final state, the intermediate states, where exotic hybrid mesons may exist, can be reconstructed. This is illustrated in the example reaction chain

$\gamma p \rightarrow p \eta_1 \rightarrow p a_1(1260)^- \pi^+ \rightarrow p \rho^- \pi^0 \pi^+ \rightarrow p \pi^- \pi^0 \gamma \gamma \pi^+ \rightarrow p \pi^- \gamma \gamma \gamma \gamma \pi^+$, where $a_1(1260)$ is a hypothesized exotic meson. There is a large number of such reactions, each with several different decay paths having predicted branching ratios².

Through the identification of the final states it is possible to use Partial Wave Analysis (PWA) to determine the intermediate states. This method looks at the various decay chains possible and from the detected particles, determine which decay method was most probable. The decays are dictated by the electromagnetic interaction, indicating that parity, charge parity, and isospin are conserved allowing for the intermediate states to be more easily determined from the final states [16].

As the decay of multiple intermediate states will result in photons being produced, as can be seen in the previous decay example, it is necessary to identify as many photons as possible and to determine their four momenta with sufficient accuracy in order to determine the intermediate states. This necessity highlights the importance

²the fraction of particles which decay by an individual decay mode with respect to the total number of particles which decay [15]

of the BCAL within the GlueX experiment and the need for its response to be well understood.

Chapter 3

The GlueX detector

3.1 Overview

In order to map out the hybrid meson spectra, the GlueX experiment was designed consisting of multiple detector components that will be used together as a system to measure the four-momenta of particles. The detector system, a near hermetic detector ($\sim 4\pi$ coverage in solid angle), primarily consists of two calorimeters, used to measure the four-momenta of photons, and a tracking system to measure the momenta of charged particles [17]. This experiment relies on studying the decay of hybrid mesons into their final states and as such, both high statistics and the ability to distinguish different final states is essential.

The entire geometry of the GlueX detector is cylindrical because of the solenoid magnet chosen; a solenoidal field will result in the very large number of electron-positron pairs produced to spiral down along the beam direction and thus not overwhelm the detectors elements. The main components of the GlueX detector are depicted in Figure 3.1 and are briefly described here [18].

- The superconducting solenoid magnet acquired from the SLAC National Ac-

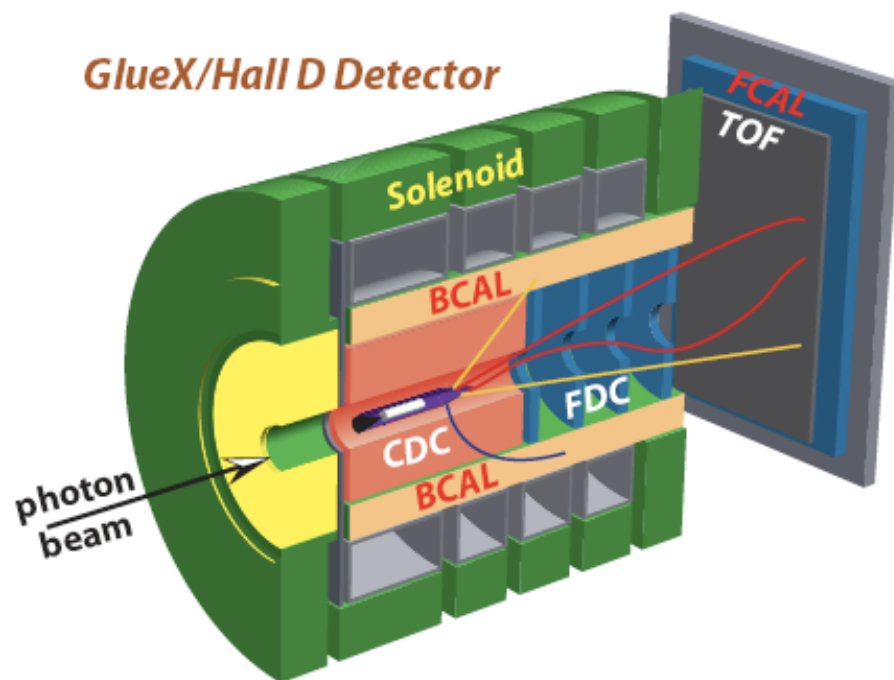


Figure 3.1: Schematic view of the side of the GlueX experiment which shows the various components and their orientation within the system. Image courtesy of the GlueX Collaboration.

celerator Laboratory, and recently refurbished at Indiana University and JLab encompasses many of the detector systems and provides a central magnetic field of 2.2 T .

- The Barrel Calorimeter (BCAL) is a barrel shaped electromagnetic sampling calorimeter primarily used to measure the energies of photons from 60 MeV to 2.5 GeV in the polar angle range of 11° to 126° .
- The Central Drift Chamber (CDC) is a straw tube chamber is used to measure the momenta of charged particles, and is located in the upstream side of the BCAL covering polar angles 20° to 170° .
- The START counter (not shown in Figure 3.1 for reasons of clarity) is used to provide timing information for charged particles. This detector immediately surrounds the target vessel.
- The liquid hydrogen target contained within a 30 cm long vessel.
- The Forward Drift Chambers (FDC) consist of four disk shaped chambers located in the downstream side of the BCAL covering polar angles 2° to 20° and will be used to measure the momenta of charged particles.
- Future Particle Identification (PID) detector.
- The Time-of-Flight (TOF) wall; which is constructed from scintillating bars connected to photomultiplier tubes (which are explained in the following chapter) and will provide timing information and particle identification on charged particles in the forward region. The TOF is placed immediately upstream of the FCAL and will cover polar angles between 2° to 11° .

- The Forward Calorimeter (FCAL); an approximately circular shaped lead glass detector used to determine the four-momenta of incident photons, located downstream of the BCAL.

As each of these components is required for the GlueX experiment to be successful, they must all be well understood and must provide known responses. Currently the BCAL, FCAL, CDC, and FDC are completely installed, with the remaining components being installed as they are being completed and delivered to the lab. The final phases of the 12 GeV electron beam upgrade at JLab are being completed, with the expected date of first beam delivery being in October 2014. The following is a brief description of the major aspects of the GlueX detector and their respective role in the project.

3.1.1 Electron Beam

The newly upgraded accelerator will accelerate and guide a beam of electrons around the beam line five and a half times (passes) to reach a final energy of 12 GeV before entering Hall D's Photon Source and Tagger building. The electrons will then strike a thin diamond wafer to produce photons via the coherent Bremsstrahlung process resulting in a linearly polarized photon beam. This wafer is oriented to produce photons in the energy range of 8 to 9 GeV, with approximately 40% of them linearly polarized (the light can be represented simply as a plane wave in two dimensions), though the wafer may be reoriented to adjust the beam energy and polarization [19]. The electrons are then removed from the photon beam through the use of a dipole magnet that steers them to a tagger spectrometer, where their momenta are recorded, a process known as tagging, in order to calculate the energy of the photons. The electrons are then directed to the electron beam dump.

The photon beam continues to the Hall D complex towards the detector systems. This beam path is shown in Figure 3.2. During this trip the photon beam passes through collimators and sweeping magnets to clean and enhance the polarization fraction of the beam and remove any electrons that may have been produced through photon interactions with the beam pipe. This process helps to preserve the linearly polarized core and minimize the likelihood of any electrons contaminating the photon beam. The final photon beam that will impinge on the hydrogen target will be have an energy between 8 to 9 GeV at an average rate of $5 \times 10^7 \gamma/\text{s}$ with 40% linear polarization [20]. The linearly polarized beam is important for separating various production mechanisms and is used for amplitude analysis to identify J^{PC} values for the produced mesons [21].

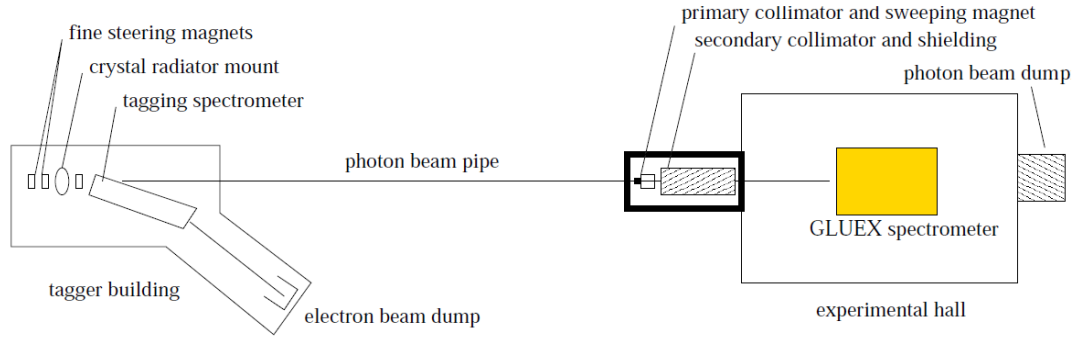


Figure 3.2: The beam line leading to the GlueX detector systems seen from above where the electron beam enters from the left. Objects are not to scale. Image courtesy of the GlueX Collaboration.

This beam will then interact with the target to produce the exotic mesons which are of interest to the GlueX experiment. These mesons will in turn decay with their final states being detected and measured by the various detectors. Any photons that pass through the target without interacting will reach the photon beam dump at the end of the beam line.

3.1.2 Charged Particle Tracking

In order to identify charged particles and measure their momentum, the CDC and FDC will be used. The CDC is a straw tube chamber consisting of a circular grid of tubes filled with an ionizing gas which will be used to detect the presence of charged particles [22]. By applying a current to the wires running down the length of the tube, an electric field is created allowing the charge from the ionization (caused by charged particles) to be collected. From this it is possible to determine the path taken by the particle as each straw will give position information for the particles trajectory as it is intercepted. The momentum of the particle can be calculated from the radius of the curvature that the particle takes through the CDC, while energy deposition per unit length (dE/dx) can be extracted from the amount of ionization that occurs. The CDC is comprised of 3522 tubes formed into a barrel, which surrounds the target with an inner radius of 10 cm and an outer radius of 55 cm. The CDC will be able to track charged particles in the polar angle region between 6° and 165° .

The FDC is in the downstream portion of the BCAL and is arranged as four disk shaped chambers, each with six planes oriented in 60° intervals to cover the full 360° . Each disk has a diameter of 60 cm, with the first three chambers spaced at equal distant apart with the fourth chamber 20 cm closer to the third. The principles governing the FDC remain the same as those for the CDC. The FDC will be able to measure charged particles in the polar angle region between 2° and 20° .

3.1.3 Calorimetry

The total energy of detected particles in the GlueX experiment is measured by the BCAL and the FCAL. When a particle enters one of these calorimeters it will deposit its energy into the calorimeter allowing the measurement of its timing, location, and

energy deposition. Only the FCAL and BCAL are able to measure the energies and momenta of photons and their primary role is to detect photons produced by the decays of π^0 and η . The BCAL can also detect charged particles. As the BCAL is a key component of the GlueX experiment and a main component of this thesis, it will be discussed later in this chapter.

The FCAL, originally the Lead Glass Detector from the Brookhaven E852 experiment, is made of 2800 lead glass detectors, each measuring $4 \times 4 \times 45 \text{ cm}^3$. These blocks are arranged in a circular formation with an approximate diameter of 240 cm. The center of the FCAL has a small gap (approximately the size of four blocks) to allow the beam to pass through the FCAL, without negatively affecting measurements. The FCAL is contained within a light tight room to prevent the detector from being overwhelmed by the room lighting and will be situated 560 cm downstream of the target.

3.1.4 Particle Identification

Proper PID is crucial to the GlueX experiment and, as such, the vast majority of components involved in the experiment are in some way able to contribute to PID. In order to provide appropriate PID, it is necessary to know a particle's energy, ionization rate, and its TOF. The first two criteria are determined by the calorimeters as well as the tracking systems while the TOF is determined by the TOF wall which covers polar angles between 2° and 11° . The TOF wall is made from two planes of scintillating bars, $2.54 \times 6 \times 252 \text{ cm}^3$ large, that are orthogonal to one another to form an XY plane. The START counter surrounding the target will initiate the TOF measurements. Limited TOF information is also available from the BCAL but only for slow moving particles ($< 300 \text{ MeV}$). Space remains between the TOF wall and

the solenoid to allow for other PID detector systems to be installed at a later date, particularly one sensitive to the differentiation between pions and kaons (such as a Direct Internal Cherenkov (DIRC) detector).

3.2 Barrel Calorimeter

The BCAL is a sampling calorimeter made from 48 trapezoidally shaped modules arranged in a cylinder or barrel shape, positioned immediately inside the solenoid's bore to an inner radius of 65 cm. Each module is made by alternating layers of 0.5 mm corrugated lead sheets and scintillating fibres of 1 mm diameter, resulting in an effective density of 4.86 g/cm³. A sampling calorimeter is one where only part of its volume is sensitive and able to detect particles and the remaining volume is an inert, high atomic number material needed to convert photons into charged particles so that they may be detected [23].

The BCAL, a key component of the GlueX experiment, and the primary contribution from the University of Regina, was based on the KLOE EmCal design [24]. Each module was built on a 3.175 cm thick aluminum plate to provide stability to the lead fibre matrix during construction and assembly. Alternating layers of lead and scintillating fibres were used with the resulting matrix shown in Figure 3.3 as seen from the end of a module. Each module is topped with a 0.8 cm thick aluminum plate to allow for mounting rails and supports to be added for the installation of the CDC and FDC. Each of the BCAL's 48 wedges is 390 cm in length, 26.1 cm radially (top to bottom) with a base (outer radius) of 11.83 cm which tapers to 8.4 cm at the top (inner radius). During my time as an undergraduate student I was employed to help with the construction of the modules.

The BCAL is shown in Figure 3.4 with several important aspects highlighted.

Its active portion is comprised of scintillating fibres¹ while the inert portion is lead and epoxy with the volume ratio of the BCAL being 37:50:13 for the lead:fibres:glue [25, 26].

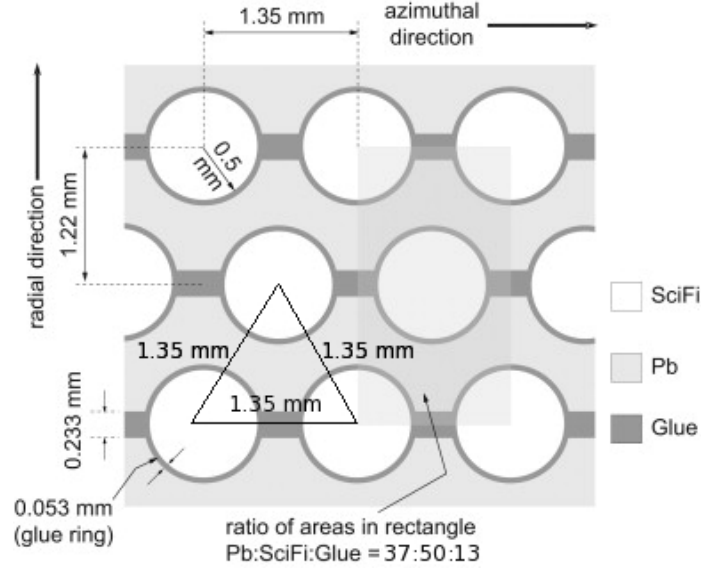


Figure 3.3: The lead and scintillating fibre matrix. Surrounding each scintillating fibre is a glue ‘ring’ with an estimated thickness of 0.053 mm. There are also glue ‘boxes’ which fills the gaps between the lead sheets. The matrix was designed such that the centers of the scintillating fibres lie on the corners of an equilateral triangle. Image courtesy of the GlueX Collaboration.

One of the primary concerns when designing the BCAL was the depth which photons will be able to penetrate into the calorimeter. The best determination of that depth is the radiation length, X_o which is expressed in centimeters. X_o is a scaling variable for the probability of Bremsstrahlung and pair production occurring, the dominant energy deposition mechanism for photons in the calorimeter [25]. It was found that the radial length of the BCAL is equivalent to $14.7X_o$ (for a 90° incident particle) and that the vast majority of energy will be deposited within the first 8 to 10 cm of the BCAL. Clearly the number of X_o increases with decreasing

¹produced by Kuraray

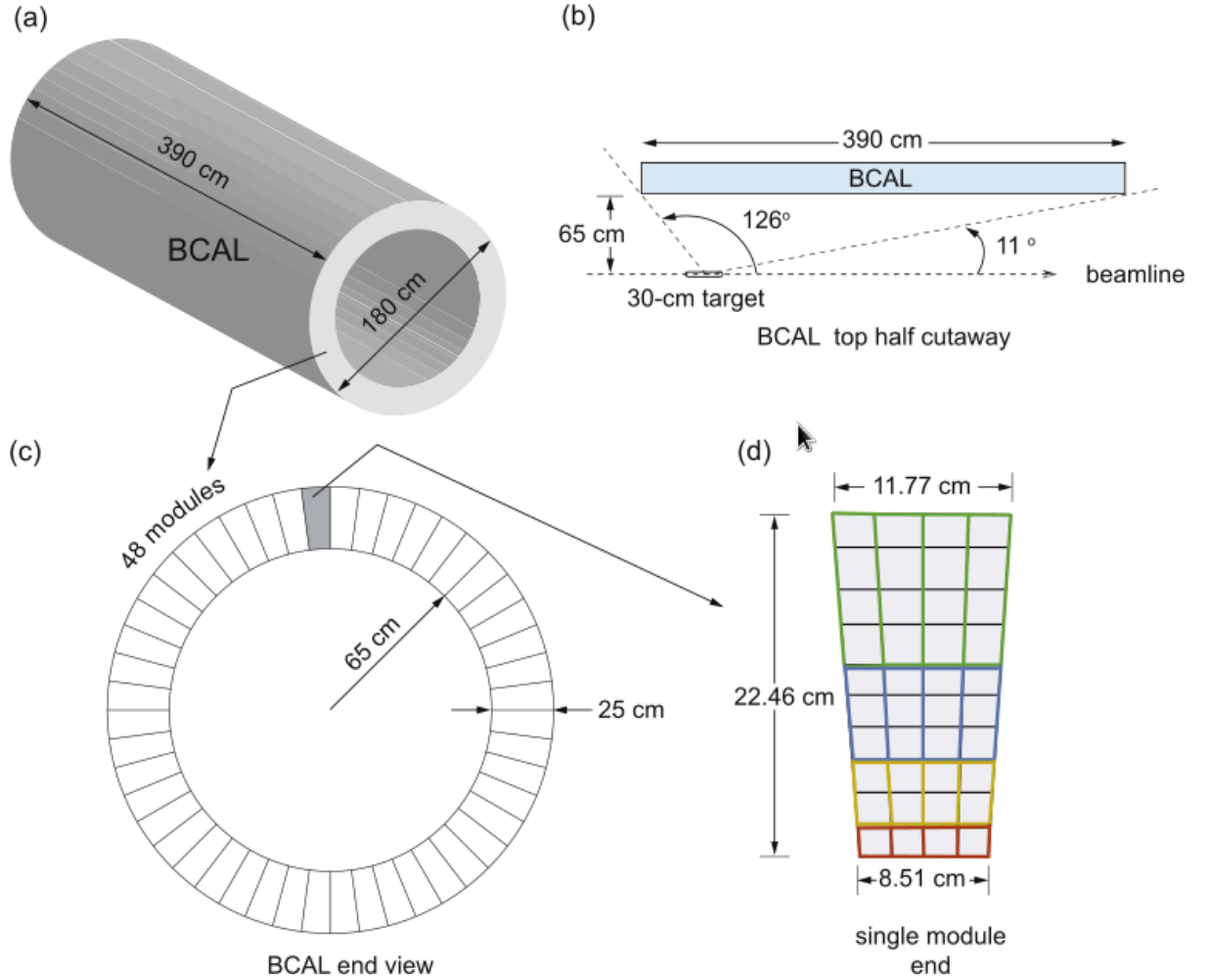


Figure 3.4: The Barrel Calorimeter. a) A view of the finished BCAL; b) a view of the top BCAL module showing the polar angles covered with respect to the target; c) end view of the 48 modules; d) end view of a single module with the readout segmentation shown. Image courtesy of the GlueX Collaboration.

polar angles reaching a peak value of $67X_o$ at $\theta=14^\circ$ before decreasing again.

From a past beam test [27], the energy resolution of a prototype BCAL module was found to be $\sigma_e/E = 5.4\%/\sqrt{E} \oplus 2.3\%$ and the time difference resolution was found to be $\sigma_{\Delta T/2} = 70ps/\sqrt{E}$. Using these values the position resolution was calculated to be $\sigma_z = 1.1cm/\sqrt{E}$ allowing the four momenta of neutral particles to be determined. It was found that these values agreed with expectations from Monte Carlo simulations [27, 28, 29].

Charged particles deposit a small amount of energy when they pass through a scintillating fibre's core, causing scintillation (through the excitation of dopants), the production of visible light. These optical photons then propagate down the fibre where are detected by appropriate photosensors.

As mentioned previously, the scintillating fibres are the active components of the BCAL. These scintillating fibres are double clad, meaning they consist of an inner scintillating core, with a thickness of 0.96 mm, and two outer layers of cladding, with diameters of 0.03 mm and 0.01 mm, respectively [30]. The core has an index of refraction of 1.60, the inner cladding has an index of refraction 1.49, and the outer cladding has an index of refraction of 1.42.

By each layer having a lower index of refraction than the previous one, more photons are likely to be internally reflected through the principle of Snell's Law, which states that

$$\theta = \sin^{-1} \frac{n_2}{n_1}, \quad (3.1)$$

where n_1 and n_2 are the indices of refraction for the first and second medium respectively and θ is the maximum angle allowing for total internal reflection.

3.2.1 Light Guides

The light guides were glued onto the faces of the module column by column using an optical adhesive². This adhesive was cured using UV light emitted from a UV lamp³ [31]. After each column of light guides was attached, a string of ten LEDs was installed, one per light guide, and bonded using the same optical adhesive. These LEDs are used for calibration purposes and will be explained in a following chapter. This process was repeated for each of the four light guide columns.

The light guides are trapezoidal in shape with a rectangular face and each set of 40 will completely cover the face of the BCAL as shown in Figure 3.5 and in Figure 3.6. Each column of light guides is identical for every module allowing for azimuthal symmetry while each row has a slightly wider base than the row preceding it, growing outwards from the center. The inner six light guides have a base height of 2.057 cm while the outer four light guides have a base height of 2.464 cm. Each light guide funnels down to a square output window of $1.319 \times 1.319 \text{ cm}^2$ [32].

²Norland NOA 87 UV Adhesive

³DTMAX BlueWave 75 UV Curing Spot Lamp

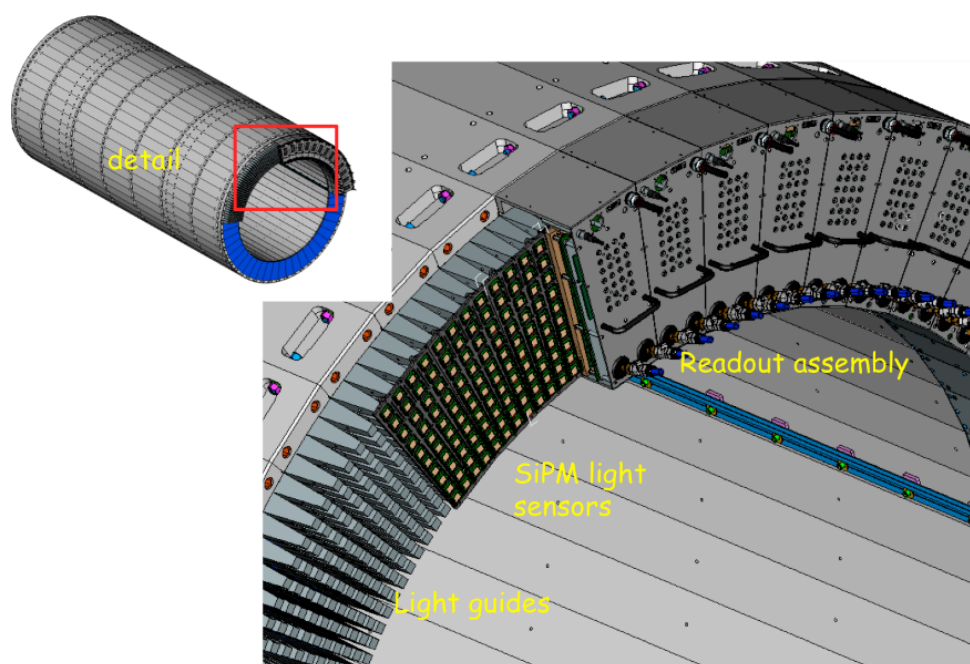


Figure 3.5: A schematic representation of the light guides on the BCAL. A few modules are shown without readout assemblies to reveal the light guides while the remaining are depicted with the readout assemblies installed. Image courtesy of the GlueX Collaboration.

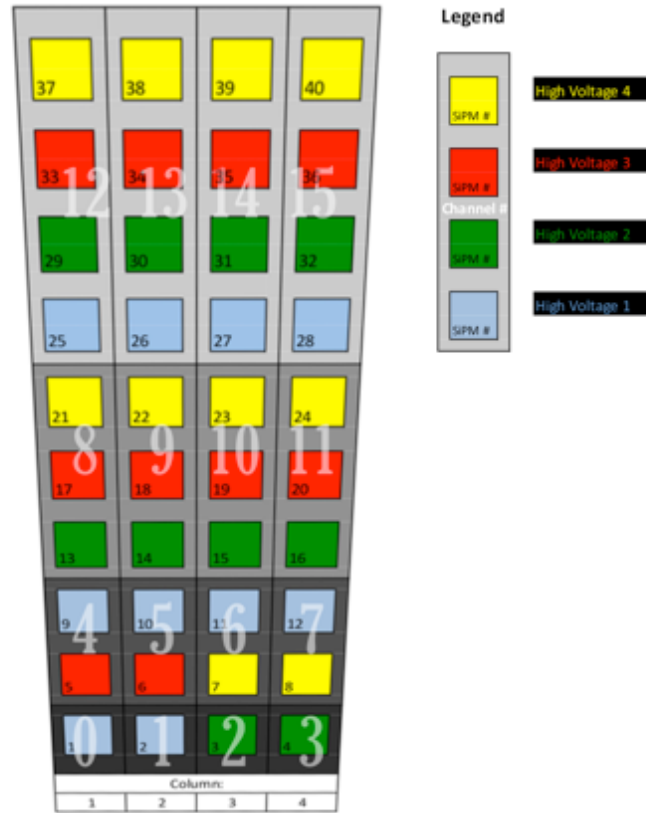


Figure 3.6: Light guides arranged on the face of the module. Each light guide is slightly wider than the one below it. Each shaded grey block (numbered 0 to 15 in white) represents the summing arrangement of light guides for the readout assemblies while the four colours represent the SiPM bias distribution system, discussed in Chapter 6. Image courtesy of the GlueX Collaboration.

Chapter 4

Silicon Photomultipliers

4.1 Introduction

The workhorse in many particle physics experiments is a device known as a photomultiplier tube (PMT), which is used to measure the number of photons incident on it. PMTs consist of a photocathode, a large number of dynodes (commonly eight to twelve), and an anode all contained within a high vacuum tube as shown in Figure 4.1 [33]. Photons striking the photocathode will release electrons which, when the PMT is powered by a high bias, will accelerate the electrons to the first dynode. This causes a shower of electrons to be produced, effectively multiplying the number of electrons present. This process is repeated until the electrons have reached the anode, where the current is measured. PMTs have two primary requirements in order to operate effectively, a high voltage supply (>1000 V), and the absence of a magnetic field, which may deflect the electrons within the vacuum tube. As the BCAL will be housed within the solenoid, the magnetic field present will prevent the operation of PMTs [34]. In order to avoid the problem that such a large magnetic field creates, a new device must be used, one that is immune to magnetic fields, such

as a silicon photomultiplier (SiPM). This immunity is largely a result of the shallow zone of sensitivity (“the depletion depth”) which is typically around 20 to 50 μm .

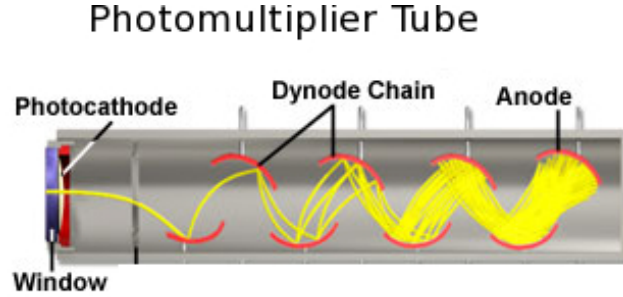


Figure 4.1: Schematic depiction of a PMT. The number of electrons is seen increasing after every dynode within the chain.

The origins of SiPM operation can be traced back to 1960 with the invention of the single-photon avalanche photodiode (APD) but it has not been until recently that large area SiPMs have come into existence [35]. A SiPM is composed of thousands of APDs arranged on a silicon substrate. Over the years, SiPMs had been developed with areas of $3 \times 3 \text{ mm}^2$ but to be practically applied, their size would need to be even larger. The GlueX experiment has been in the forefront of this demand, requiring SiPMs with a total area of $1.2 \times 1.2 \text{ cm}^2$ comprised of tiling $3 \times 3 \text{ mm}^2$ SiPM cells together. To fully understand the abilities of these large area SiPM arrays, it is beneficial to study its most basic component, the APD.

4.2 Avalanche Photodiode

Unlike traditional PMTs, APDs are solid state detectors that operate using semiconducting materials arranged in a p-n junction. A p-n junction consists of a heavily doped n-type semiconductor, with an excess of electrons, and a larger, less heavily doped p-type semiconductor, with a deficit of electrons, (or vice versa), sandwiched

together; the interface is known as the depletion zone as there is practically no net charge (as seen in Figure 4.2) [33]. When operated in forward bias, electrons flow from the n side to the p side, which is far easier for the electrons than operating in reverse bias. When operated in reverse bias, as done in the GlueX experiment, the electrons and holes (defined as the lack of an electron) are pulled towards their respective terminals resulting in a larger depletion zone [36]. As such, only a small leakage current flows through the semiconductor until the reverse bias is large enough to cause the junction to break down. At the point of breakdown, the avalanche effect arises, allowing the creation of electron-hole pairs through collisions in the depletion zone. This results in a shift from the proportional zone, where current cannot cross the depletion zone, to the Geiger zone, where current can flow freely, as seen in Figure 4.3. It is within the Geiger zone that the APD is able to function. The breakdown voltage is dependent on temperature as a higher temperature results in a large vibrations within the crystal lattice increasing the likelihood of an electron colliding with a nucleus before it can achieve sufficient energy to cause an avalanche [37].

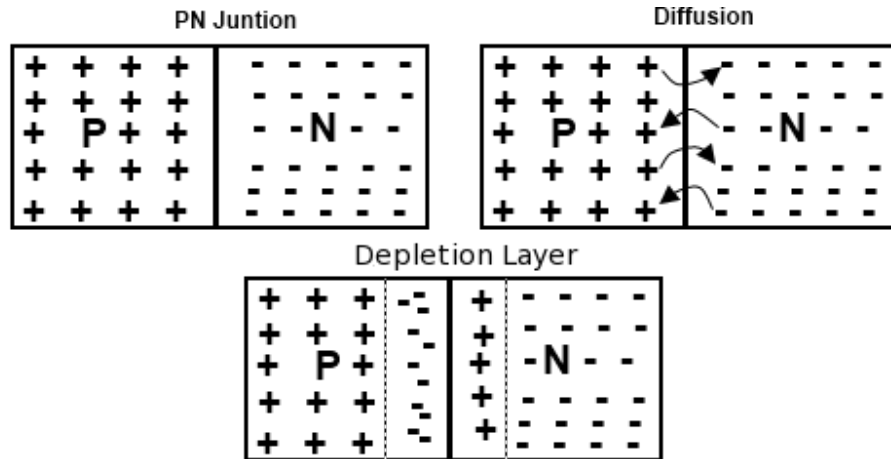


Figure 4.2: Schematic view of a p-n junction and the formation of the depletion zone [38].

Initially, photons incident on the face of the APD will release an electron via an internal photoelectric effect. When the reverse bias is less than the breakdown voltage these photoelectrons will fail to pass through the junction, however, when the bias is above the breakdown voltage, electron-hole pairs can be created. These released electrons are then accelerated by the breakdown voltage, gaining energy. Even over such a small distance (in the range of μm for the depleted zone) the relatively small potential provided by the reverse bias, around 70 V, can create an electric field in the order of 10^6 V/m [12]. This accelerated electron can impart enough energy to excite additional electron-hole pairs leading to an avalanche of electrons. This is known as a Geiger-type discharge. The greater the voltage supplied to the APD above its breakdown voltage (termed the overbias), the greater the chance of creating such an avalanche, which results in an increase in the gain, defined as the amount of charge generated from a single photoelectron.

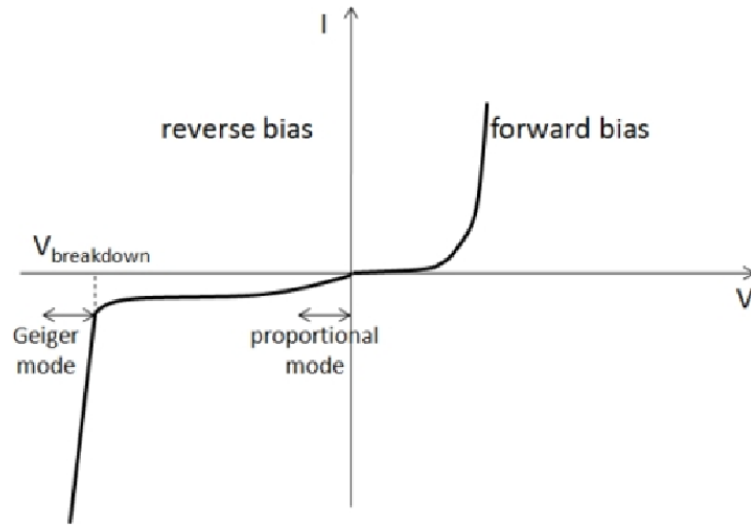


Figure 4.3: When operated in reverse bias mode, an APD will briefly conduct a current proportional to the voltage (leakage current) until the depletion region becomes too great an obstacle at which point a plateau is reached. The current remains constant as a function of voltage until the Geiger mode occurs at which point the current falls drastically.

In order to stop, or quench, an avalanche, it is necessary to drop the bias either by an external resistor or through quenching electronics. By quenching the avalanche, one can ensure that the current generated from a single APD is nearly constant regardless of how many photoelectrons produced the avalanche as seen in the following equation, in which the gain of an APD is determined from:

$$G = \frac{C(V - V_{br})}{q} \quad (4.1)$$

where G is the gain, C is the APD capacitance, V is the supplied voltage, V_{br} is the breakdown voltage (making $V - V_{br}$ the overbias), and q is the charge of an electron. The gain will be nearly constant for any avalanche that is initiated such that each APD acts as a Geiger counter. As such, every time an APD is activated a photon is counted.

Single APDs are unable to distinguish between a single photon and multiple photons, which prevents them from being useful to determine differing photon fluxes. However, by combining thousands of APDs together into a single array, it is possible to go from a binary input to an analog signal output.

4.3 Silicon Photomultipliers

A SiPM is essentially a large array of thousands of APDs, referred to as pixels, assembled on a silicon substrate. In order to determine the number of photons incident on a SiPM, the binary signal of every APD is summed together to form an analog signal.

The design of a standalone APD is modified slightly when used as part of a larger SiPM array. A single pixel of such a SiPM array can be seen in Figure 4.4. The

p-n junction is placed on a silicon substrate that has also been treated with a p-type dopant [39]. This creates another, larger depletion zone, between the pixel and the silicon substrate which will have the same properties as in a standalone APD. Any avalanche that is created in this depletion zone will be quenched by a silicon resistor connected to the pixel dropping the voltage below the breakdown voltage. Aluminum connectors are used to transmit the signal from each pixel, allowing the summed signal to be read, and from this, the total number of photons can be determined.

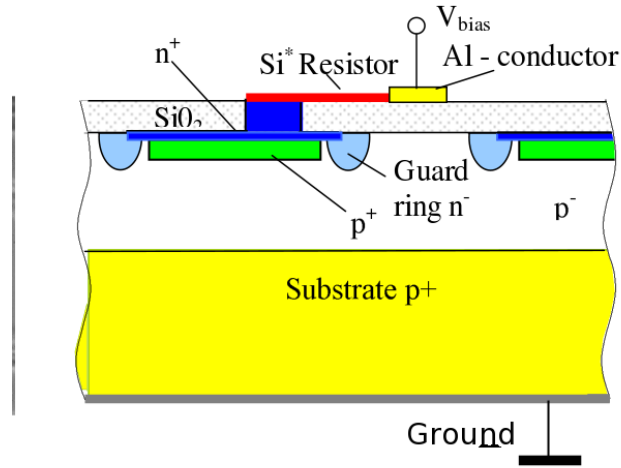


Figure 4.4: The schematic view of a single SiPM pixel [40].

SiPMs are more advantageous than single APDs for a variety of reasons including:

- a larger size while still remaining compact
- an analog signal opposed to binary due to the summing of many APDs
- it is not necessary to detect every photon incident on it; so long as the photon detection efficiency is known it maintains a useful signal

4.3.1 Photon Detection Efficiency

One of the critical characteristics of a SiPM is how efficient it is in its ability to detect incident photons, which is expressed as its photon detection efficiency (PDE). The PDE is defined as the ratio between the number of pixels fired (or activated) in a given SiPM to the number of incident photons. The PDE depends on several intrinsic factors and is given by

$$PDE(\lambda, V, T) = QE(\lambda) \cdot F \cdot \epsilon(\lambda, V, T) \quad (4.2)$$

A typical SiPM will have a PDE of 10% - 25%, with this value being dependent on the intrinsic quantum efficiency of the pixel, $QE(\lambda)$, the fraction of photosensitive material to the whole area (geometric fill factor), F , and the avalanche probability $\epsilon(\lambda, V, T)$. The geometric fill factor is simply the ratio of the photosensitive area of the SiPM to its total area [41].

The quantum efficiency of the silicon APD is the ratio of emitted electrons to incident photons, which excite an electron-hole pair in a pixel. Since different energy photons will have different probabilities of causing an electron-hole pair, the quantum efficiency will also be energy dependent. However, the energy of a photon is dependent on its wavelength by

$$E = \frac{\hbar c}{\lambda} \quad (4.3)$$

meaning the quantum efficiency is wavelength dependent. This relationship can be seen in Figure 4.5, where the PDE is plotted as a function of wavelength [42].

The last factor, the avalanche probability, is how likely a self-sustained avalanche will occur if a photoelectron is created. This is predominantly affected by the bias supplied to the SiPM, or more specifically, the overbias. As the overbias is increased,

the likelihood that a photoelectron will be accelerated sufficiently to excite additional electrons in the depletion zone increases. This does not mean, however, that the over-bias can be raised as much as possible due to fact that the noise, or dark rate (which will be discussed later), will also rise. It is possible to find the optimum overbias for a specific SiPM by minimizing the noise to signal ratio and thus optimizing the PDE.

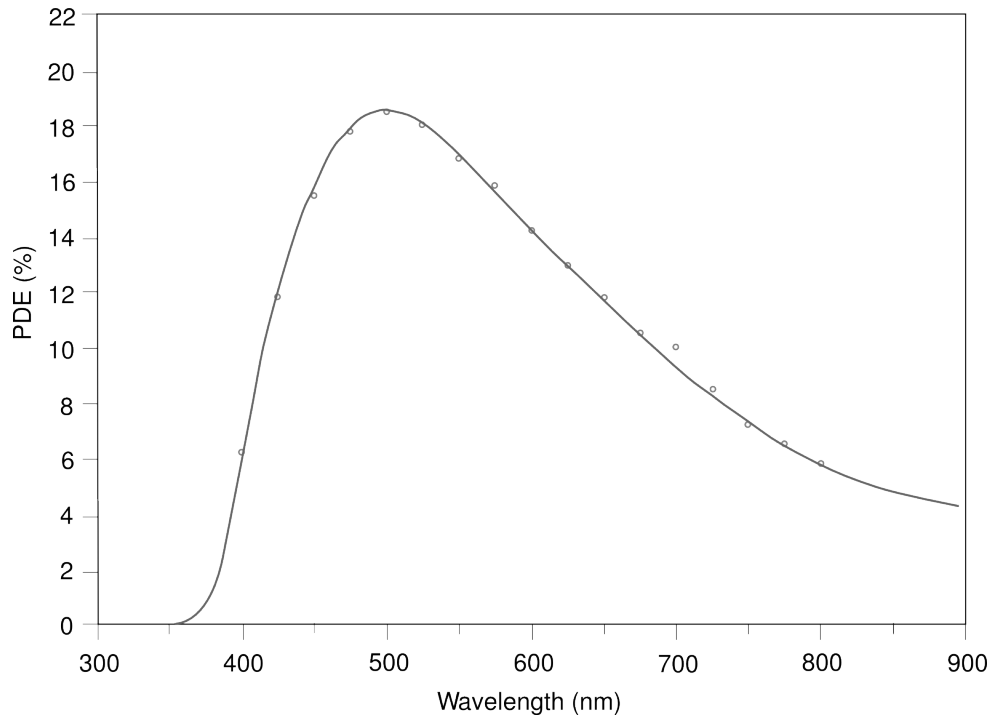


Figure 4.5: A typical APD response comparing PDE to wavelength [12].

4.3.2 Recovery Time

As previously discussed, SiPMs are able to effectively detect single photons but this process is not instantaneous, as each pixel requires some time to undergo the avalanche and then undergo quenching so that the next incoming photon can be detected. This process depends on the amount of time it takes for the pixel to

recharge its capacitor and acts as the limiting factor to the speed of the detector. The recovery time tends to be around 50 ns for most SiPMs [44]. If every pixel is fired simultaneously the recovery rate will be 50 ns for the SiPM as a whole leading to a minimum count rate of 20 MHz. The likelihood of every pixel firing simultaneously however is not very high, thus pixels that have not been previously fired are able to detect incident photons, even while previously fired pixels are still recovering. In other words, the effective counting rate can be much higher.

4.3.3 Linearity

The linearity of a SiPM relies on the firing of a pixel being associated with only one incident photon. Multiple photons striking the same pixel may go uncounted as the pixel may still be recovering, resulting in a non-linearity between the signal and incoming photons. When the number of photons incident on the SiPM is low, each photon detected should result in a linear response. The current measured is proportional to the incoming photon flux and is found using the equation

$$I = \frac{dN_\gamma}{dt} \cdot \eta \cdot G \cdot q \quad (4.4)$$

where N_γ is the incident number of photons, η is the photon detection efficiency, G is the gain, and q is the charge of an electron. Thus, so long as the SiPM operates in its linear region it is trivial to determine the number of photons incident on it.

If multiple photons are incident on the same pixel before it has had a chance to recover its photosensitivity, then, only the first photon will be counted. This will make the SiPM's response non-linear. As the photon flux increases, this non-linearity will become more significant as the likelihood of multiple photons striking the same pixel increases. This will result in the current being increasingly disproportionate to

the number of incident photons.

4.3.4 Dynamic Range

The dynamic range is defined as the range between the largest and smallest signals expected to be measured. For a SiPM, the dynamic range depends on the PDE, the number of pixels in a device, and the number of incident photons. The number of pixels fired is simply the product of the number of incident photons, N_γ , and the PDE, η . When divided by the maximum number of pixels fired (all the pixels firing simultaneously), m , the dynamic range is found, which, as the PDE is always less than one, must also be less than one

$$\frac{N_\gamma \cdot \eta}{m} < 1 \quad (4.5)$$

One of the requirements placed on the SiPMs for the GlueX experiment is that the dynamic range is greater than the maximum number of photons expected for any SiPM within its recovery time. It has been estimated that upwards of 30,000 photons may reach a single SiPM within the inner portion of the BCAL, where the vast majority of events are expected. With a PDE of 20% and a pixel count of 57600 the dynamic range of any given SiPM is above 250,000 photons, well above the highest expected number.

4.4 SiPM Noise

When dealing with any detector system it is important to understand the sources of noise that may occur in the signal. There are two possible sources of noise for SiPMs, the dark rate, and optical cross talk.

4.4.1 Dark Rate

The largest source of noise in SiPMs is the dark rate, which is the number of false photons counted per second. These false photons are not incident on the SiPM but instead are caused by avalanches that have been generated in the p-n junction depletion zone. These avalanches can be caused by spontaneous emissions of electrons from within the p-n junction, either through random thermal processes, such as Auger recombination¹, or by flaws or impurities in the silicon, a process known as the Shockley-Read-Hall process².

While some causes of dark rate are intrinsic to the SiPM, dark rate is also temperature dependent. The dark rate of a SiPM can be reduced by as much as a factor of 10 with a decrease in temperature of 20°C [12]. As such, cooling the SiPMs to a low temperature will reduce noise significantly.

The dark rate is also a function of overbias and sometimes this is a linear relationship [45] while other times non-linear [46]. A measure of the dark rate can be determined by recording the SiPM data in the absence of light.

4.4.2 Optical Cross Talk

Another type of noise is caused by a phenomenon known as optical cross talk. As electrons pass through the material of the SiPM, there is a chance that one of them may produce new photons in the process. With the pixels grouped in a relatively small area there is a chance that these photons may pass into another pixel and cause a new avalanche which results in multiple pixels firing for a single photon.

In order to reduce the likelihood of cross talk, grooves or trenches can be cut into the SiPM face between pixels to act as an optical barrier for the photons [47].

¹The spontaneous emission of an electron from an atom.

²The excitation of an electron from a defect within the silicon.

4.4.3 GlueX Specifications

In addition, with an increase in temperature, the breakdown voltage will increase linearly and in the case of the Hamamatsu SiPMs³, by a factor of $0.056\text{V}/^\circ\text{C}$ [48].

This is dependent only on the size of each pixel and the inactive spacing in the SiPM array. For the SiPMs provided by Hamamatsu, this fill factor is around 0.60.

An estimation of the limit to the linear region of a SiPMs response can be found by assuming each of the 57600 pixels, the number of pixels in the SiPMs used by GlueX, is being fired simultaneously at a frequency inverse to that of the pixel recovery time. So long as the SiPM is operated within its region of linearity the number of photons can be directly determined, but outside of this region this is not the case, which is why it is crucial to remain in the region of linearity. The specifications for the GlueX BCAL readout require better than 10% linearity [41]. Based on the number of pixels in each array, the number of arrays in a cell and the energy deposition by “physical” photons in each cell, the linearity criterion is expected to be met in this experiment.

³Hamamatsu Model S12045(x).

Chapter 5

Readout Assemblies

5.1 Introduction

When an exotic meson decays within the BCAL, photons are produced that propagate down the scintillating fibres to be detected by the SiPMs at either end. Each BCAL module is equipped with two readout assemblies, one for either end, each of which houses 40 SiPMs arranged in a 4 x 10 grid. In order for the light to be transmitted from the scintillating fibres to the SiPMs, acrylic light guides were used, with every SiPM being paired with a light guide. Between each light guide and its corresponding SiPM is a 1 mm air gap, which is shown in Figure 5.1 along with the inner components of the readout assembly [49].

5.1.1 Readout Assemblies

Each end of a module is equipped with a readout assembly as shown in Figure 5.2. The design of the readout assemblies was based on several factors:

- the need to conveniently and reproducibly mount or dismount (for mainte-

*Cutaway View
Single SiPM Shown*

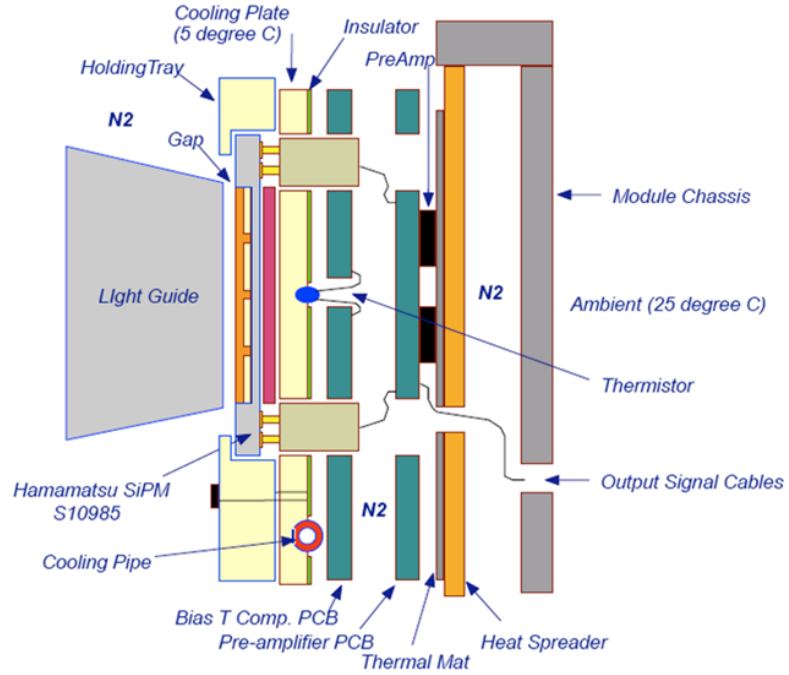


Figure 5.1: A cutaway view of a single SiPM, showing its position relative to the light guide, and the assorted components within the readout assembly. The insulator, cooling pipe, cooling plate, thermal mat, and heat spreader are all part of the overall cooling system designed to keep the SiPMs operating at a near constant 5°C. The preAmp, bias temperature comp. PCB, and pre-amplifier PCB are all components of the signal collection and processing from the SiPM. More details are included in the text. Image courtesy of the GlueX Collaboration.

nance) 40 SiPMs at a time

- the need to maintain a uniform air gap between the SiPMs and their respective light guides thus maintaining an equivalent geometry for purposes of light transmission
- the avoidance of mechanical stresses on the windows of the SiPMs as well as the complexity of spring-loaded mechanical systems by not having physical contact between the light guides and SiPMs

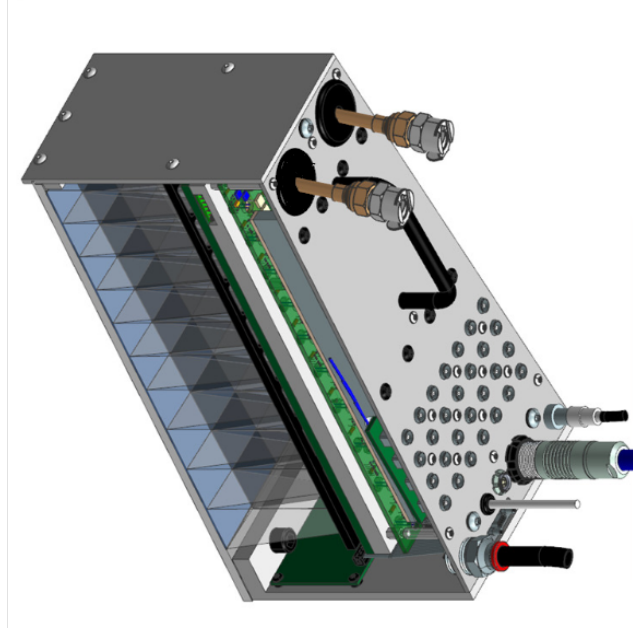


Figure 5.2: Readout assembly attached to the face of a module. The light guides are visible on the left. The BCAL module is not shown for the purpose of clarity. Image courtesy of the GlueX Collaboration.

The readout assemblies are divided into three main regions: the SiPMs, the cooling system, and the readout electronics. The reason for this separation is that the SiPMs must be kept as near 5°C (the operating temperature of the experiment) as possible and, as the readout electronics will give off heat, a cooling system is placed

between them to maintain a constant temperature. Dry nitrogen gas will be used to maintain a dry environment, minimizing the risk of condensation on any electronics.

The SiPMs are divided into four readout rows for the readout assemblies as can be seen in Figure 5.3. The innermost row (with respect to the beam line) includes a single layer of SiPMs, with each SiPM in a column read out separately. The second row consists of summing the SiPMs in layers two and three together on a per column basis. The third row sums layers four, five, and six, while the fourth layer sums the remaining four SiPMs, again, on a per column basis. The purpose for such a summing scheme is threefold; first, the bulk of the energy from the photon shower is deposited in the six innermost layers (the first half of the module), and this is approximately true regardless of incident photon angle. Therefore a finer segmentation was required in this region. Second, the cost to read out each individual SiPM was beyond the budget allocated. Third, since little energy is deposited in the outermost region a coarser segmentation optimized the energy collection.

As a result, there are a total of 16 separate energy readout channels on the back of each readout assembly (as was seen in Figure 5.2) which can be connected to electronics and eventually a Data Acquisition (DAQ) system (16 per end, with 2 end of 48 modules results in 1536 total energy outputs). In addition to the energy measurements, the SiPMs are also able to provide timing information which, when interpreted by a time-to-digital converter (TDC) is able to determine when a pulse arrived with respect to a common timing origin. The fADC can also be used to give timing information as will be explained later. This is important to know as the timing difference between the upstream and downstream ends for the same pulse can be used to determine the location within the module where an event occurred. TDC information is not collected for the cells involving the summation of four SiPMs due

to cost constraints (as such there are 12 readouts per end, with 2 end for 48 modules resulting in 1152 TDC outputs).

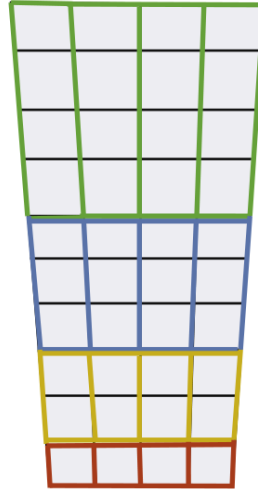


Figure 5.3: 1:2:3:4 segmentation of the BCAL module. Each colour grouping shows a different summing group where the bottom row has no summing, the next row up sums two SiPMs and so on. Image courtesy of the GlueX Collaboration.

At the heart of the readout assemblies are the 40 SiPMs on each end (3840 total). Such a large number of voltage sensitive devices will always exhibit a variation in performance. With the GlueX experiment demanding a high level of uniform responses amongst its detector systems, it is crucial to sort the SiPMs in such a way as to offer the most consistent response for every readout assembly as possible.

All design decisions reported in this section were taken collectively by the GlueX Collaboration and Jefferson Lab Management.

5.2 SiPM Binning

It is of paramount importance that the supply voltage of the SiPMs be as close as possible to their own unique specified voltage as defined by the manufacturer.

To supply each of the 3840 SiPMs with their own optimum voltage would require a power supply for each SiPM. However, this was not financially feasible; instead only 48 power supplies are employed, each with eight channels as well as distribution panels so that one channel can supply ten SiPMs. In order to optimize the SiPMs with a common voltage as close to their specified voltage as possible, they were binned in groups of ten based on their manufacturer's specified voltage and, using a compensating circuit comprised mainly of resistors as seen in Figure 5.4, the supplied voltages were thus brought closer to the specified voltages. The design and construction of the boards was done in house at Jefferson Lab.

The upper and lower sections of this circuit contain resistors that are used to reduce the supplied voltage; each group of four resistors is referred to as a trim. The middle portion of the circuit consists of a thermistor and linearizing resistor, which will compensate for temperature fluctuations between 5°C and 20°C and form a linear dependence on temperature based on the temperature coefficient of 56.0 mV/°C. Without the thermistor and linearizing resistor, the temperature dependence would not be linear making it far more difficult to apply temperature corrections.

The requirements for the binning procedures are such that each SiPM must be within 10 mV of its specified voltage and that the current must be held as near constant for all SiPMs as possible, while still maintaining the first requirement. The thermistors utilized by the GlueX experiment depend on the current to remain constant in order to correct for temperature fluctuations. As such, a balance must be reached that allows the voltage to be brought as close to the specified value as possible without sacrificing too much control on the temperature dependence: the more strictly the voltage is controlled, the greater the deviations in current for each SiPM, which could result in the temperature term to no longer remain constant.

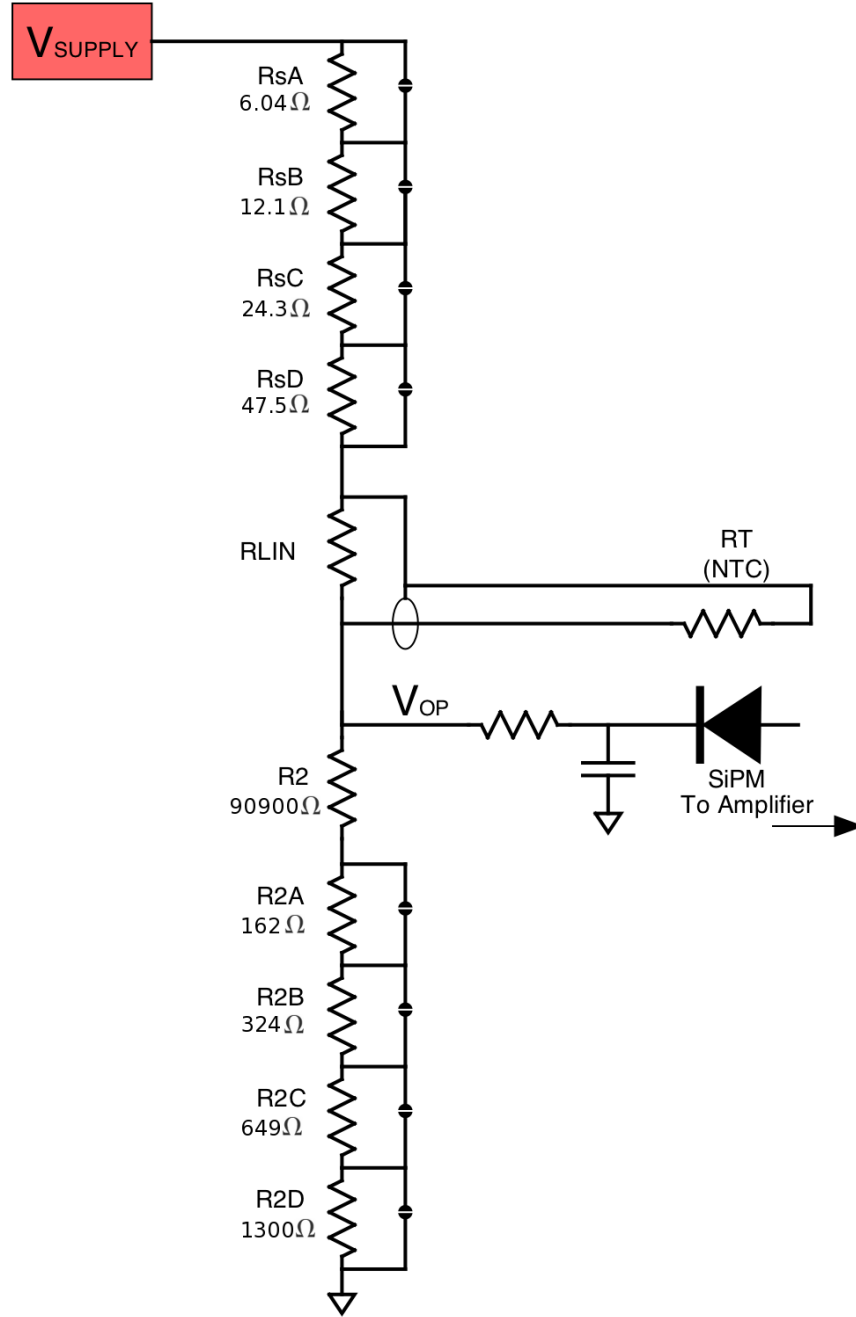


Figure 5.4: The electronics circuit designed to help match the voltage supplied by the power supply to the operating voltage of the SiPM. It is possible to utilize only a subset of the eight resistors by applying jumpers to remove specific resistors from the circuit. Image courtesy of the GlueX Collaboration.

An added challenge to this procedure is that the eight resistors must be the same for every board in order to reduce manufacturing and assembly costs. As such, these eight resistors must span the entire specified voltage range of all 3840 SiPMs.

5.2.1 Determining the Resistors

The first step of this process was to determine the desired current for the circuit. It was found to be 0.7682 mA at 5°C, determined from the formula

$$I_o = \frac{-TCV_d}{\frac{B_o R_{Lin} U^2}{T^2 [R_{Lin} + U]^2} - \frac{B_o R_{Lin} U}{T^2 [R_{Lin} + U]}} \quad (5.1)$$

where

$$U = R_{T_o} e^{B_o(\frac{1}{T} - \frac{1}{T_o})} \quad (5.2)$$

TCV_d is the Temperature Coefficient of Voltage which expresses the relation between the voltage and temperature of the system; a value of 56.0 mV/°C provided by Hamamatsu. The terms B_o , R_{T_o} , and T_o are all properties of the thermistor chosen where B_o is the resistance to temperature fluctuations, R_{T_o} is the resistance at a calibration temperature, and T_o is the calibration temperature. These values are $B_o=3980$ K, $R_{T_o}=5.00$ K Ω and $T_o=298.15$ K. Lastly, R_{Lin} is the resistance of the linearizing resistor, 6490 Ω , and T is the temperature of the circuit. As such, equations 5.1 and 5.2 are dependent only on temperature T as the other terms have been fixed. As the experiment is meant to be kept nominally at 5°C, the current is expected to remain constant. With the current for each SiPM known, and the specified operating voltage, it is trivial to determine the resistance that each SiPM would need in order to match the ideal voltage and supplied voltage.

A large, precision resistor of 90900 Ω was chosen as it was as close as possible

to the lowest resistance needed determined through $R=V/I$ where V is the lowest specified voltage and I is the desired current. This allowed the trim resistors the greatest flexibility in covering the whole range of resistances needed. It was decided to cover this range by using binary steps; the maximum resistance needed minus the precision resistor was divided by 2, 4, 8, and 16 and those values were used to populate the first trim resistor.

The voltage supplied to each group of SiPMs was found using the equation

$$V_s^{Ideal} = I_o \frac{R_{Lin} R_{T_o} e^{B_o(\frac{1}{T} - \frac{1}{T_o})}}{R_{Lin} + R_{T_o} e^{B_o(\frac{1}{T} - \frac{1}{T_o})}} + (I_o - I_{Leak}) R_2^{actual} \quad (5.3)$$

where $R_{2actual}$ is the resistance from the first trim resistor.

I_{Leak} is an estimate of the leakage current from the SiPMs. Currently this value is estimated at 1 μA though as the SiPMs become more irradiated during the course of this experiment this may grow to as large as 20 μA . The maximum voltage of each group is what is applied to all ten SiPMs, with the second trim resistor used to bring the other nine SiPMs as close to their specified voltage as possible. This was done through an iterative process to minimize the deviation in current, while keeping the supplied voltage as close as possible to the ideal voltage for each SiPM. It was found practically that again, a binary stepping method produced the best results for the second trim.

The resistors that best satisfied the requirements are listed in Table 5.1. Using these, it was found that the current varied by at most 1.5% from its specified value and all SiPMs were within the 10 mV requirement as seen in Table 5.2 and shown in Figure 5.5.

Table 5.1: The resistors used to match a SiPM's optimum voltage to the supplied voltage.

Resistor	Value (Ω)		Resistor	Value (Ω)
R_2A	162		R_sA	6.04
R_2B	324		R_sB	12.1
R_2C	649		R_sC	24.3
R_2D	1300		R_sD	47.5

Table 5.2: The number of SiPMs within a certain voltage of their ideal value and the total percentage within this range.

Within: (mV)	# of SiPMs	% of total
1	31	0.81
2	42	1.09
3	54	1.41
4	45	1.17
5	1791	46.64
6	1271	33.07
7	425	11.07
8	181	4.71
Total	3840	100

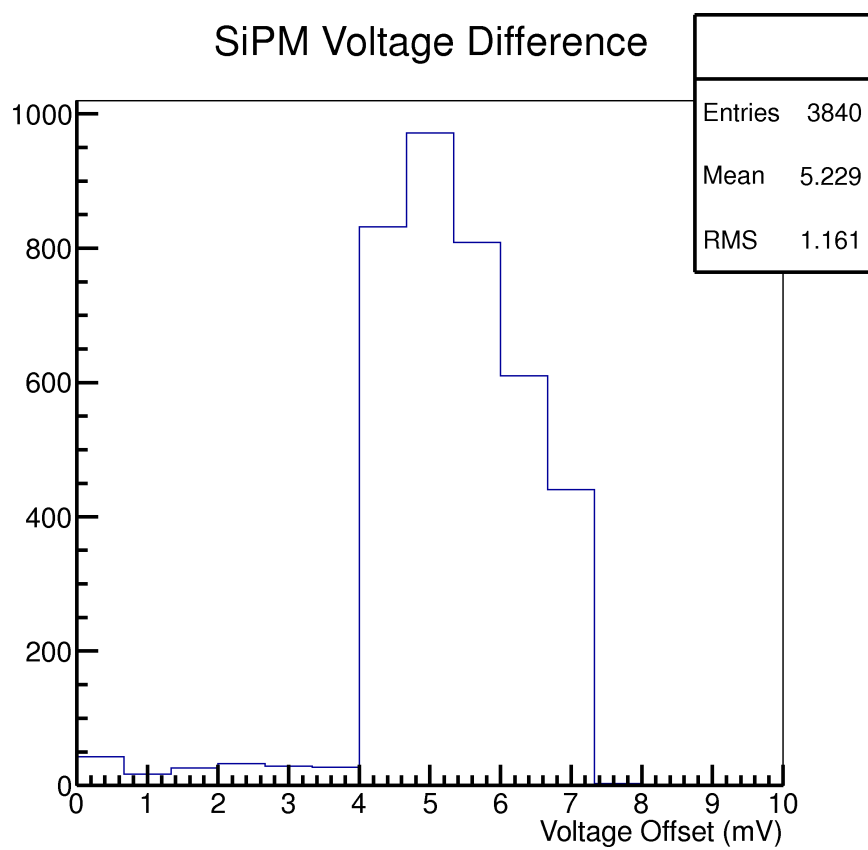


Figure 5.5: The difference between the supplied voltage and the specified voltage for the GlueX SiPMs.

Chapter 6

Module Calibration Tests

6.1 Introduction

It is important that the entire BCAL offers a uniform and well understood response for the duration of the GlueX experiment (approximately 5 to 10 years). As the light guides will be considered part of the module, tests must be done to determine their light transmission. Specifically, the uniformity of the light guide gluing was evaluated using LEDs¹ as well as cosmic rays that generated the light in the calorimeter.

In order to test each module, two separate experiments were conducted to ensure that each light guide was glued properly on to the module, offering a consistent interface for light to traverse and that each LED was functioning properly and oriented properly. The first of these tests was conducted by powering a single string of LEDs and powering a single set of SiPMs (grouped such that no two SiPM within the same summing group are powered together) such that only specific LEDs were being detected. As the majority of the readout cells have some amount of summing between light guides, it is necessary to power at most one LED per summing group in order

¹Bivar Model SMS1105BWC InGaN LEDs

to test its output. A grand total of 32 individual measurements were done to check each LED individually. Details of this test are explained later in this chapter.

The second test was conducted using cosmic radiation to determine:

- the absolute energy deposition, dE , in each SiPM layer
- the ratio of energy deposition in the four layers (and if it scales as expected)
- the track reconstruction on an event-by-event basis
- the timing resolution of each module

These results were compared across all the modules to ensure uniformity in the BCAL as a whole. Cosmic radiation provided an easy and convenient method to penetrate such a thick detector in order to calibrate each module. Muons deposit a specific amount of energy per unit length within the fibres. For a vertically oriented module, vertically incident muons should deposit 22.9 MeV of energy in the first layer, 45.8 MeV in the second, 68.7 MeV in the third, and 109.3 MeV in the fourth. This scaling is caused by the 1:2:3:4 summing scheme employed on the readout assemblies.

The energy deposition was determined through the formula

$$E = \frac{f * L * (dE/dx)_{mip}}{s} \quad (6.1)$$

where f is the fibre volume fraction (the fraction of fibres to the total volume), assumed to be 0.5, $(dE/dx)_{mip}$ is the amount of energy deposited per unit length by cosmic muons which is 2 MeV/cm, s is the sampling fraction, previously found to be 0.095 [50], and L is the cell length which is simply the height of each summing group. Clearly equation 6.1 then assumes that all the cosmic muons enter vertically into the module.

6.2 Experimental Setup

In order to conduct these measurements the experimental setup seen in Figure 6.1 was utilized. This setup allowed for both LED and cosmics testing to be carried out with nearly the same setup allowing for quick transitions between experiments. The same readout assemblies consisting of the same SiPMs were used for every test on the modules to ensure that it is the modules and light guides being tested and not the various readout assemblies (which will be studied at a later date). The 32 energy readout channels are connected to two 250 flash ADC's (fADC) while the 24 TDC readout channels are connected to two F1 TDC units utilizing the same type and length cables as for the fADC. The fADCs convert the signal sent from the SiPM into an energy spectrum while the TDCs determine the times that signals arrived at each SiPM as well as the trigger. By ensuring all the cables are of the same length, all the signals should arrive at the electronic crates nearly simultaneously and any timing offsets seen are likely caused by actual physical properties of the test. Each individual test was run using a specially designed slow controls program known as EPICs² which allows each grouping of SiPMs to be powered individually, as well as allowing the user to enter the temperature of the system which automatically adjusts the supplied voltage [51]. The readout assemblies were kept at near constant temperature of 16°C through the use of an ethyl glycol and water mixture being circulated through the cooling pipes within the readout assemblies.

Each module was covered in several layers of black plastic and blankets in order to block out ambient light from interacting with the SiPMs. Given the size of each module as well as the time constraints on the experiment it was impractical to construct or find a light tight room to conduct these experiments and these measures

²Experimental Physics and Industrial Control System

proved to be effective in blocking out the light from affecting the measurements.

To control the LEDs, an external trigger was used which flashed the LEDs at an approximate rate of 300 flashes per minute. The cosmic test was triggered when cosmic rays pass through a scintillator block measuring 30 cm by 15 cm placed under the center of the module as was shown in Figure 6.1. For purposes of symmetric positioning and timing information, this trigger was approximately centered underneath the module.

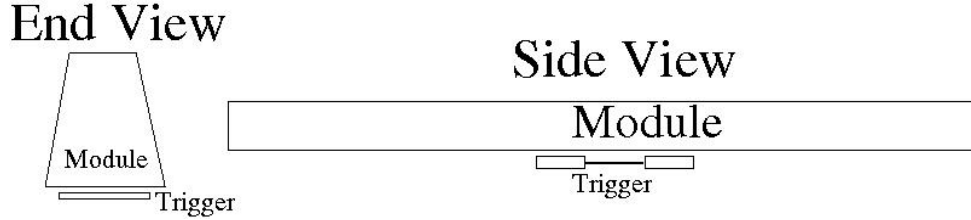


Figure 6.1: Schematic drawing showing the end and side views of the experimental setup for the LED and cosmic tests.

6.3 LEDs

6.3.1 Monitoring system

In order to monitor the stability and the relative gain of the SiPMs over the duration of the GlueX experiment, an LED system will be used periodically to illuminate the SiPMs allowing a relative gain check to be made. It is necessary to monitor the stability of the SiPMs throughout the experiment as any shifts in their relative performance would affect final state calculations. The SiPMs will be calibrated such that their gains are as near uniform as possible and that the response of each unit is well understood. However, this calibration is useful only so long as a SiPM maintains its initial gain. In order to continuously update the calibrations for the BCAL, it is

necessary to monitor the gains of all SiPMs at least once per day to allow for any corrections to be made to the calibrations, the latter generated from the detection and reconstruction of π^0 's and charged particles.

The LED monitoring system consists of a single global controller board for each end of a module which is responsible for the four strings of LEDs. Each LED is mounted on an LED board which controls that specific LED.

An LED system was designed for monitoring purposing for a variety of reasons including [49]:

- The ability to selectively fire groups of LEDs to allow for individual SiPM evaluation. The LED power distribution system was designed to allow a single string of 10 LEDs to be activated independently. In addition to this, the power distribution system for the SiPMs is divided into four, essentially orthogonal, independent subsystems as shown in Figure 6.2. By powering an individual set of SiPMs the summing effects can be avoided and only that specific SiPM will be tested.

BIAS DISTRIBUTION

37	38	39	40
33	34	35	36
29	30	31	32
25	26	27	28
21	22	23	24
17	18	19	20
13	14	15	16
9	10	11	12
5	6	7	8
1	2	3	4

BIAS 1
BIAS 2
BIAS 3
BIAS 4

Figure 6.2: The bias distribution used for the SiPM readout modules. The bottom row is the single SiPM layer. The colour legend is explained by the smaller graph at the bottom. Image courtesy of the GlueX Collaboration.

- To have a lower cost than other monitoring systems used in the past while offering a simplified design allowing for easier and quicker repairs. Other designs, such as a laser combined with a fiber distribution method, were considered but discarded due to cost, size, and difficulty to maintain.
- To exhibit a compact design, necessary given the limited space between light guides. An LED based system is ideal for this as a single LED is quite compact versus lasers or other illumination systems, allowing them to be mounted directly on the light guides while the control boards can be mounted under the light guides. As the LEDs are attached directly to the light guides, there is no need for additional fibres to propagate light from a different light source, reducing the construction costs and minimizing possible electronic failures in the future.
- To generate a low heat and electromagnetic footprint which may effect the SiPMs. Minimal energy consumption will result in low electromagnetic interference and minimal heat production, where both of these could alter the SiPM readings which are in close proximity. After many tests of a SiPM in close proximity to a control board, a pulser board, and strings of LEDs, no detectable noise was found from any of the elements of the LED monitoring system. The temperature effects were studied for the LEDs and it was found that a variation of $\pm 2^{\circ}\text{C}$, the range allowed by the cooling system attached to the readout assemblies, resulted in a variation of less than 14 percent in the SiPM signal [49].

The LEDs used in the monitoring system were mounted onto a pulser board as seen in Figure 6.3a. The LEDs were then glued into the pockets (or bores) located 3.4 cm from the base of the module with a depth of 2 mm and a diameter of 4 mm on the

side of each light guide shown in Figure 6.3b. Figure 6.3c is after having glued the LEDs onto a column of light guides.

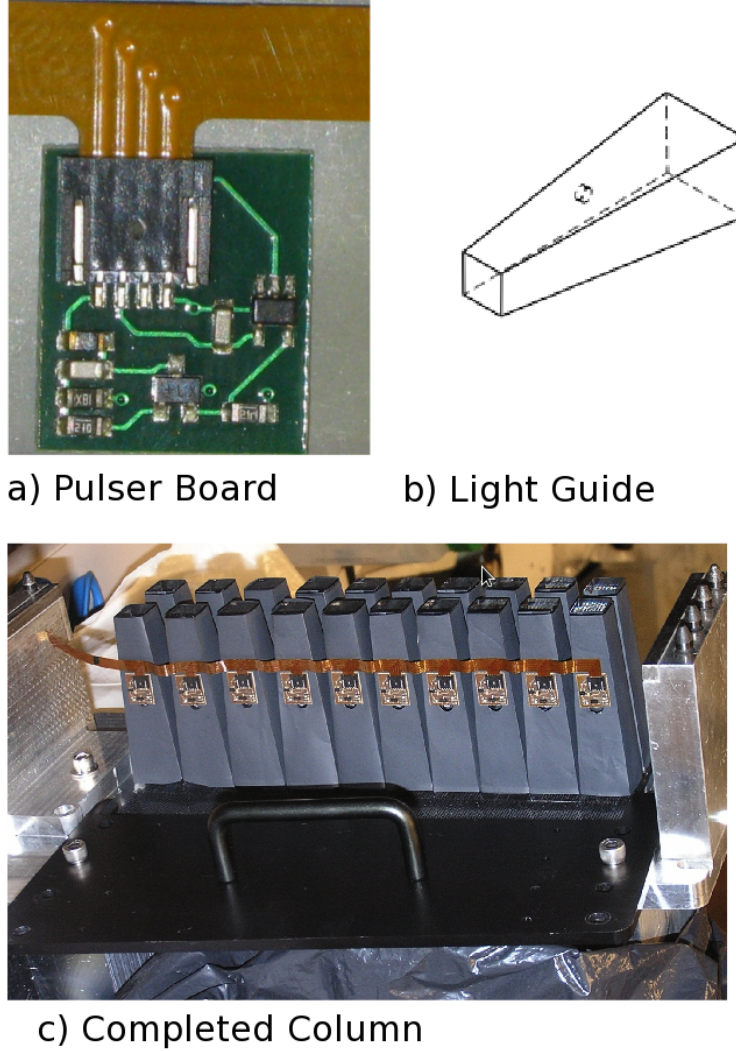


Figure 6.3: a) The pulser board used to control the LED. b) A schematic view of the bore in the light guide where an LED is glued. c) A finished row of LEDs glued into place. Metal plates were bolted onto the sides of each module during the gluing phase in order to line up the light guides during gluing [49].

Ideally, each LED would be inserted such that 75% of the light emitted would travel down the long axis of the light guides to the modules. This was done such that after attenuation the far to near ratio (upstream versus downstream) should be

approximately 1. However, realistically it is not possible to have each LED inserted perfectly into the bore resulting in some variance throughout the measurements. As such, the monitoring will be based on relative values, how much the signal changes over time from its original value, as opposed to an absolute value of the intensity of each signal. Measurements were taken at both ends of the modules to determine the fraction of light that travels down the fibres to the SiPMs located to the far side of the module, relative to the remainder of the light that is reflected from the light guide module interface back to the near SiPMs. This allowed for the calculation of a ratio between far and near (or equivalently upstream and downstream based on the orientation each module will be placed in the BCAL) to be calculated. A benefit of this reflection is that it provides a redundancy for the monitoring system, in other words, should an LED fail it is possible to still monitor the gain of the SiPM through the LED on the opposite side. This also provides a means to check the modules over time for any degradation of the fibres [49].

6.3.2 LED Measurements

Each light guide and LED pair was tested in order to ensure that no significant air bubbles were left behind when the light guides were glued onto the module and that each LED worked and was oriented correctly within the bore. Any significant distortions in the glue surface will cause a reduction in light transmission.

As previously mentioned, the LEDs and SiPMs are powered in two separate schemes and by cycling through all sixteen combinations of SiPM bias (four separate bias controls) and LED strings (four separate control strings) it is possible to measure each of the SiPMs individually. This process was repeated for both ends of the module resulting in 32 separate measurements.

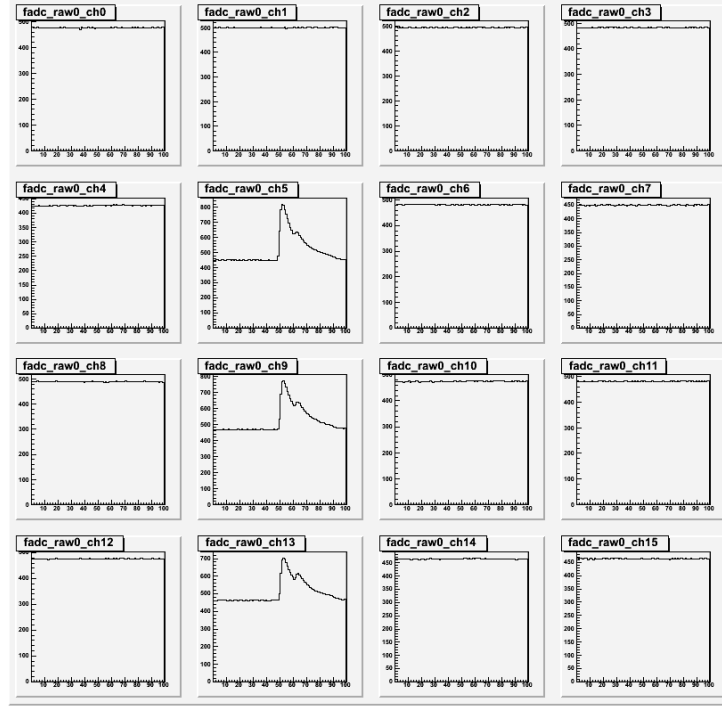
Each measurement consisted of approximately 300 events, where an event is a single LED flash. A single randomly chosen pulse was used for analysis, while a selection of the remaining 300 events was used as a visual check to ensure that the signals are consistent. Usually only the first 30 to 50 events were considered unless a signal was too low, or distorted, at which point additional events were used to check if an aberration is randomly occurring for a short period of time or was consistent amongst all the events.

The randomly chosen event was visually inspected to ensure that the pulses agreed with expectations. The first characteristics that were checked were to ensure that there was a signal in each of the expected cells with no significant signal in any cell expected to be empty. This was done by comparing the event to Table 6.1, which lists the cells that should have a signal given a specific bias configuration. A typical event is shown in Figure 6.4, which was produced by having the downstream end powered with SiPM bias 3 and LED string 2 drawing power. Typically a peak height of approximate 350 ADC counts above the baseline, or about 260 MeV, was expected for the LED adjacent to the SiPM while the far SiPM was expected to record a pulse height of approximate 900 ADC counts above the baseline, or about 680 MeV. These values did fluctuate depending on the orientation of the LED within the light guide, the quality of scintillating fibres within the module, the percentage of fibres covered by the light guide, and the quality of the glued surface. Should a pulse adjacent to the light guide have a peak height much less than 350 ADC counts, or no detectable pulse whatsoever, while the remaining peaks within the event appeared normal, that LED was likely improperly inserted into the bore. However if all the pulses were significantly lower than expected it likely meant an issue with the power distribution system, either the controller board was faulty or the ribbon cable was damaged. It

Table 6.1: User’s Guide for powering various LED and SiPM strings and the expected result. Note: Column 1 downstream (“down”) for the light guides corresponds to column 4 on the upstream (“up”).

Up/Down	Light Guide Column	SiPM Bias	Active Cells
Up	1	1	7, 15
Up	1	2	3, 11, 15
Up	1	3	11, 15
Up	1	4	7, 11, 15
Up	2	1	6, 14
Up	2	2	2, 10, 14
Up	2	3	10, 14
Up	2	4	6, 10, 14
Up	3	1	1, 5, 13
Up	3	2	9, 13
Up	3	3	5, 9, 13
Up	3	4	9, 13
Up	4	1	0, 4, 12
Up	4	2	8, 12
Up	4	3	4, 8, 12
Up	4	4	8, 12
Down	1	1	0, 4, 12
Down	1	2	8, 12
Down	1	3	4, 8, 12
Down	1	4	8, 12
Down	2	1	1, 5, 13
Down	2	2	9, 13
Down	2	3	5, 9, 13
Down	2	4	9, 13
Down	3	1	6, 14
Down	3	2	2, 10, 14
Down	3	3	10, 14
Down	3	4	6, 10, 14
Down	4	1	7, 15
Down	4	2	3, 11, 15
Down	4	3	11, 15
Down	4	4	7, 11, 15

Downstream End



Upstream End

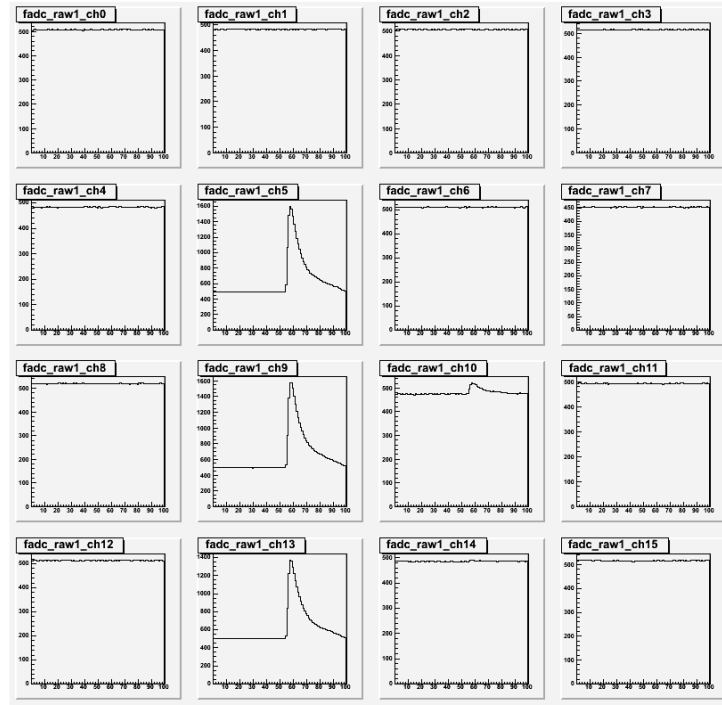


Figure 6.4: The signal generated for the downstream end when SiPM bias 3 and LED string 2 are turned on. The small pulse seen in cell 10 of the upstream end is characteristic of the small pulses seen from optical cross talk.

was found that all cases of consistently low pulses was caused by a broken cable (which was replaced) and were not caused by the controller board.

It is not uncommon to see a small pulse, in the range of 50 to 100 ADC counts, in a cell adjacent to a pulse caused by optical cross talk. This is caused by the placement of the LED on the side of the light guide and the fact that each light guide does not necessarily cover the whole fibre along its borders and some of these fibres are shared with adjacent light guides. The amount of cross talk varied depending on various factors but was usually a few percent on the near side and could be as large as 10% on the opposite side [56].

Another common feature observed in the near side spectra is a small peak superimposed onto the larger peak at a time difference of approximately 40 ns as shown in Figure 6.5. This secondary pulse is most likely caused by a reflection at the interface between the fibres and light guide at the opposite end which then reflects back to the near side. This is supported as the speed of light within the module is 17.04 cm/ns resulting in approximately 44 ns for the light to traverse the module twice, (there and back again). This phenomenon was observed in approximately 90% of the spectra.

If a single peak was found to be at a lower ADC value than all the others in that run, the LED light guide pair in question required repairs. A visual check was done on the light guide to ensure it was clear with no cracks or marks and the glue interface was clear and mostly free of air bubbles. If the surface looked cloudy or otherwise marked, the light guide was removed from the module and cleaned after which the light guide was reattached to the module and a second test was conducted. However, if the surface was clear then the intensity of the LEDs was increased to the point where it was visible with the naked eye. A visual check was done to ensure that the

LED was firing and that its intensity was as bright as the other LEDs in the same string. If the LED was not functioning or appeared significantly dimmer than its companions the LED was removed and replaced. It was not uncommon for the LED to remain within the bore after the pulser board was removed, requiring the light guide to be replaced as well. Unfortunately, given the proximity of neighbouring light guides, it was often necessary to remove at least one adjacent light guide to gain access to the one requiring repairs. After repairing a light guide, or replacing an LED, that side of the module was completely retested to ensure nothing had been damaged during repairs.

Detailed and systematic evaluation of electronic connections, ground traces and components was carried out by the Jefferson Lab Electronic group independently of this study.

6.3.3 Results

The vast majority of tests were successful on the first attempt with less than 5% of these measurements needing to be repeated. Only a small subset of these failed tests resulted in all pulses being significantly lower than expected. All of these cases was remedied by replacing the ribbon cable supplying power to the LED string. The remaining number of failed tests consisted of a single peak being significant lower than expected. Reattaching the light guide or replacing the LED was found to remedy the problem resulting in all LEDs pulses offering an acceptable signal. These tests will be repeated after the modules have been assembled into the BCAL to ensure that no cables or light guides had been damaged during the installation phase.

6.4 Cosmic Radiation

6.4.1 Preliminary Preparation

In order to determine the response of each module to the low flux of incident minimum ionizing particles (MIPs), they were subjected to at least twelve hours of cosmic testing. MIPs (cosmic muons) are ideal for the task of determining a module's response as the amount of energy deposited per unit length of a scintillator is well known. The energy measured in each of the 32 readout cells can then be compared to the expected amount of energy deposited from muons and quantitative measurements of each module's response can be recorded for future calibrations.

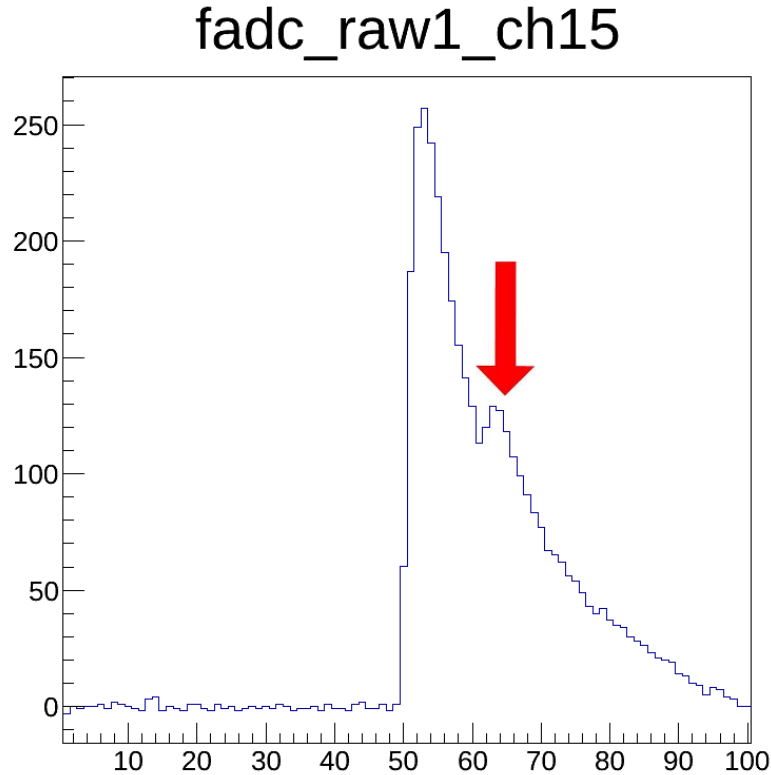


Figure 6.5: A reflected signal seen on the near SiPM when conducting LED tests.

Initially the data must be pruned such that only events with clearly defined tracks through the module were used, removing both null events, where a muon passed through the trigger without having traversed the module, and showers, where an interaction occurred within the module resulting in multiple pathways. The requirements on the tracks were made even more strict by mandating that only nearly vertical tracks that passed through a single column (vertical) of light guides was considered. This is done to simplify the analysis by ensuring the energy from each well defined portion of a path is read by a single SiPM grouping. The signal of each of the 32 cells, as shown in Figure 6.6, was analyzed for each event to determine the quality of the signal. In order to determine if a cosmic event was acceptable for further analysis two different sets of criteria were used. The first set of criteria used in order to determine the quality of the events was to check each column for a usable signal in each of the four cells, while each cell in the adjacent column(s) contained no usable events as seen in Figure 6.7 such that all the energy is contained to a single column. In order for a pulse to be defined as a usable signal it must be nine ADC counts above the baseline, an electronic based offset used to determine signal fluctuations. Nine ADC counts above the baseline, or 0.5 MeV, was chosen as the threshold to maximize the number of events accepted as can be seen in Figure 6.8. A threshold lower than nine reduced the number of acceptable events by considering background noise as a signal in one of the veto channels, while a threshold above nine begins to remove legitimate events. Those events that have passed these criteria are labeled as clean events.

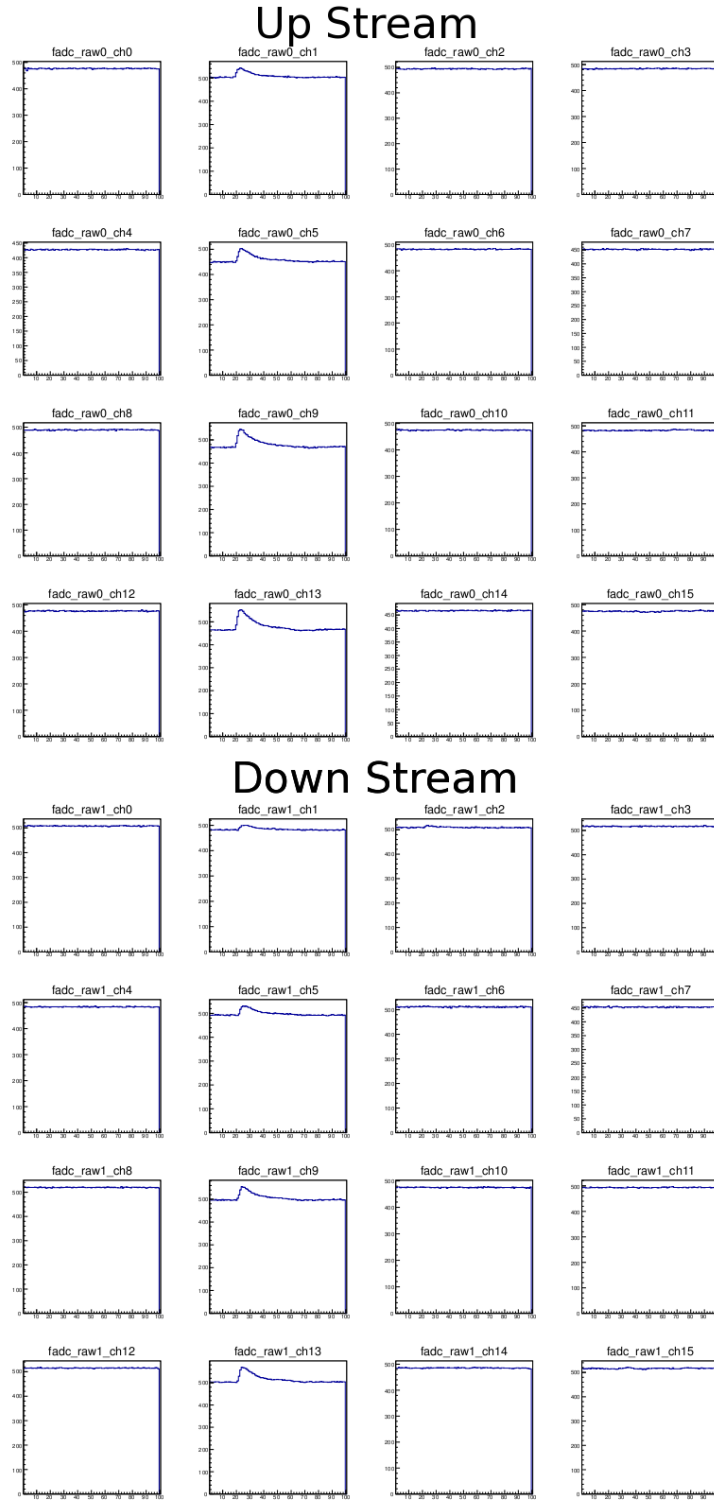


Figure 6.6: A cosmic muon passing through a single column within a module.

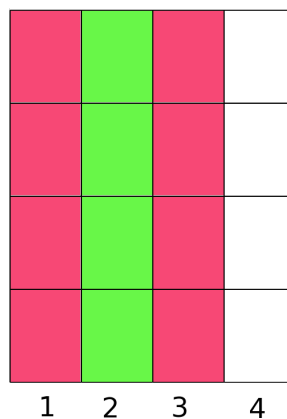


Figure 6.7: For a vertically incident cosmic muon in column 2 we expect a signal in all the green cells and no signal in any of the red cells (columns 1 and 3).

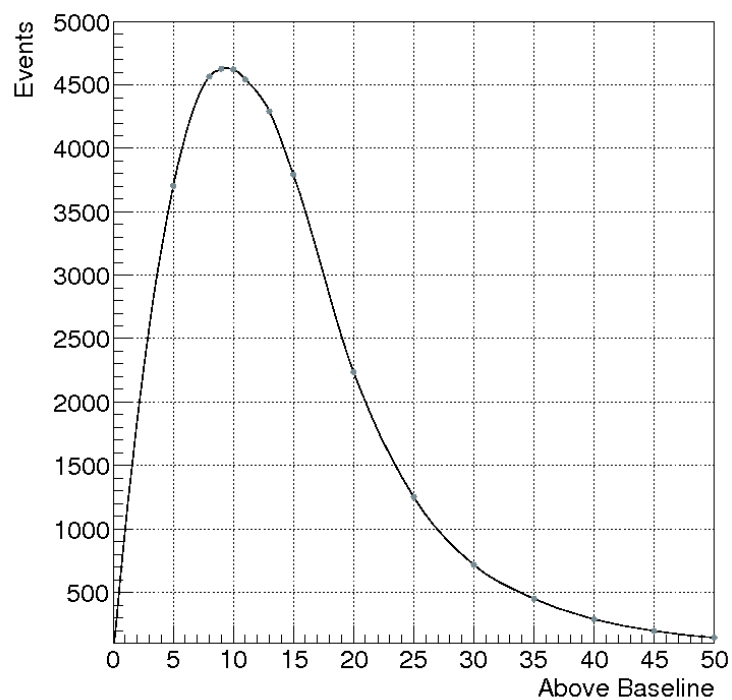


Figure 6.8: A threshold above the baseline was determined by varying the size of the threshold and determining the number of events that were deemed “clean”.

6.4.2 Energy Determination

Having sorted the data into those with clean tracks, the next step was to determine the energy deposition for each layer and compare this to the calculated values. It was the bulk of the pulse that is of interest however, so only the pulse between the 15th and 70th timing bins was analyzed as depicted in Figure 6.9. The x scale represents the time in 4 ns increments with the energy sampled every interval. These thresholds indicate the time frame that is of interest for analysis. The beginning placement was chosen to cut off the majority of the flat baseline before the signal arrived. The end placement was chosen by incrementing the marker in 5 bin increments starting from 20 until the resulting sigma/mean value was minimized. With the interval of interest determined, the pulse could be analyzed by summing the ADC channels together to determine the area under the curve, as well as determining the maximum peak height.

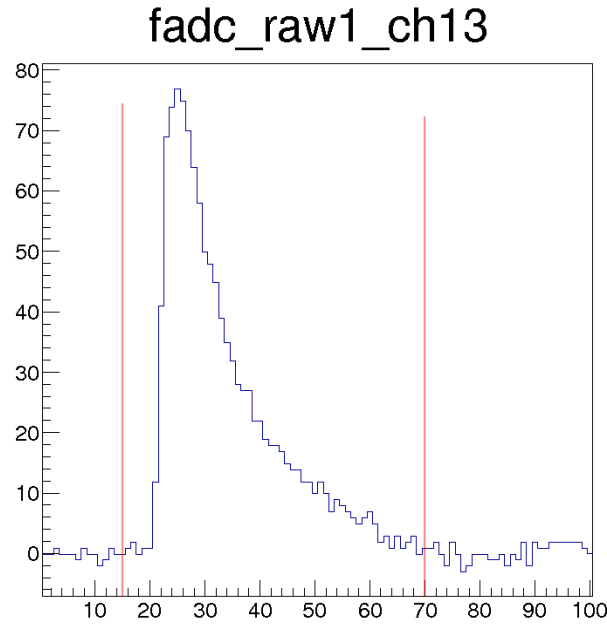


Figure 6.9: The integration window was set between bins 15 and 70.

The energy information gathered by the SiPMs expresses the energy only in terms of ADC channels which, while it does provide a relative comparison between modules, it does not provide any absolute energy reading. In order to convert ADC channels to MeV, a plot was made for each cell of the maximum peak height versus the summed ADC channels for each event, with an example of this plot shown in Figure 6.10. The electronics (gain) were designed such that a 1 MeV particle would have a peak of 1 ADC bin height when run at 1.2 V overbias. As the SiPMs were operated at 0.9 V overbias during the cosmic tests this term scaled down to 0.75 MeV/ADC peak. By combining the slope of maximum peak height versus ADC sum and the 0.75 MeV/ADC peak a conversion factor is determined allowing the summed ADC channels to be converted to MeV. The procedure was conducted for each of the modules and it was found that they each had very similar slopes as shown in Figure 6.11. This conversion factor was determined to be 0.0583 MeV/ADC sum for every module.

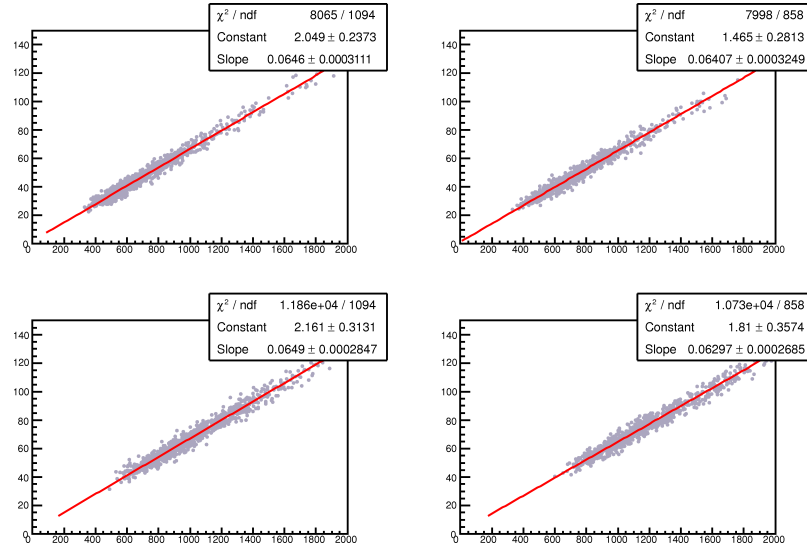


Figure 6.10: Summed ADC versus maximum peak height. The four panels shown are the central four readout cells of a single module with the remaining cells being consistent.

6.4.3 Timing Information - TDC

An obvious issue with the described experimental setup is that, while the calculations to determine the expected energy deposition assumes cosmic radiation passes through the detector vertically, sloped tracks do occur. In order to correct for these sloped tracks, the timing information must be used from the readout assemblies in order to determine the path the particle took when traveling through the module. Since the scintillation light will be emitted from where the particle interacted with the fibre, it is simply a matter of determining when the signal reached each readout cell, and from the difference in times, determine where an event occurred.

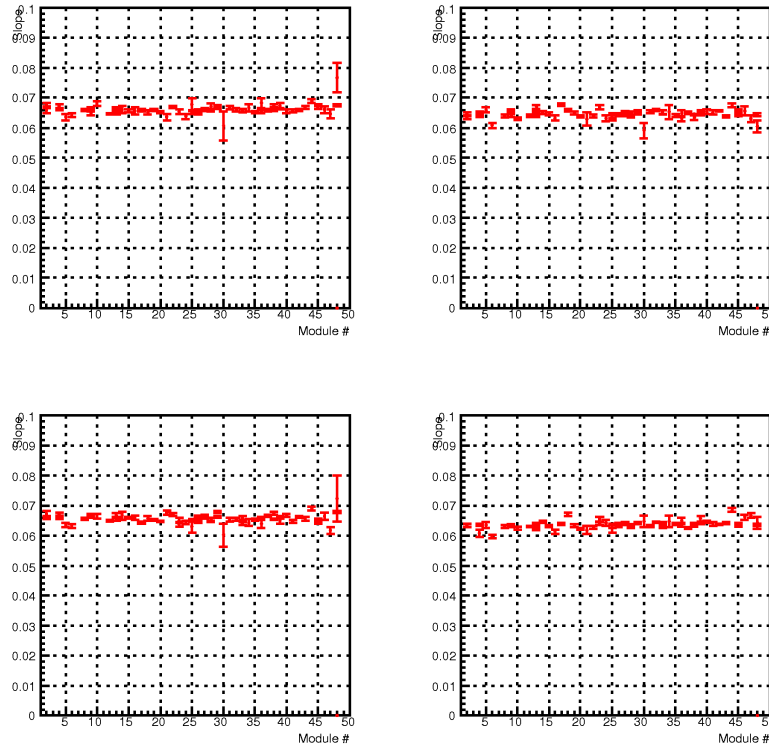


Figure 6.11: Slope (determined from summed ADC versus maximum peak height) versus module number. The four central readout cells are shown for clarity sake with the remaining cells being consistent.

The preliminary plan had been to utilize the TDC information collected from the readout assemblies in order to complete this task. The timing information for each pulse was collected from each of the eight readout cells that had been activated and from there the downstream side was subtracted from the upstream side. In order for the timing information to be accurate however, it was necessary to apply a correction known as a time walk correction. This is because leading edge discriminators were used, which result in the timing information that has a dependence on the pulse height of the signal [52]. A typical plot is shown in Figure 6.12a, where the timing difference is plotted against the peak height of the upstream pulse. This distribution is fit with the function

$$F(p) = a + \left(\frac{b}{p + c} \right)^d \quad (6.2)$$

where p is the peak height, a is the linear baseline term, b is a scaling term, c is the peak offset term, and d is the exponential term.

Which is subtracted from the data and replotted against the peak height of the downstream pulse shown in figure 6.12b. Again the same function is fit against the new distribution and subtracted to result in Figure 6.12c, which no longer shows a dependence on peak height. This procedure also normalizes the timing information to correct for any artificial shifts in the timing differences caused by the electronics. By applying the correction to both the upstream and downstream sides separately, the dependence of energy is accounted for in both sides.

Unfortunately, when the experiment was prepared the TDC information was not expected to be needed, and as such, the thresholds used to sort the signal from the noise were set too high causing most of the needed information to be removed. It was found that TDC information was collected for both the upstream and downstream

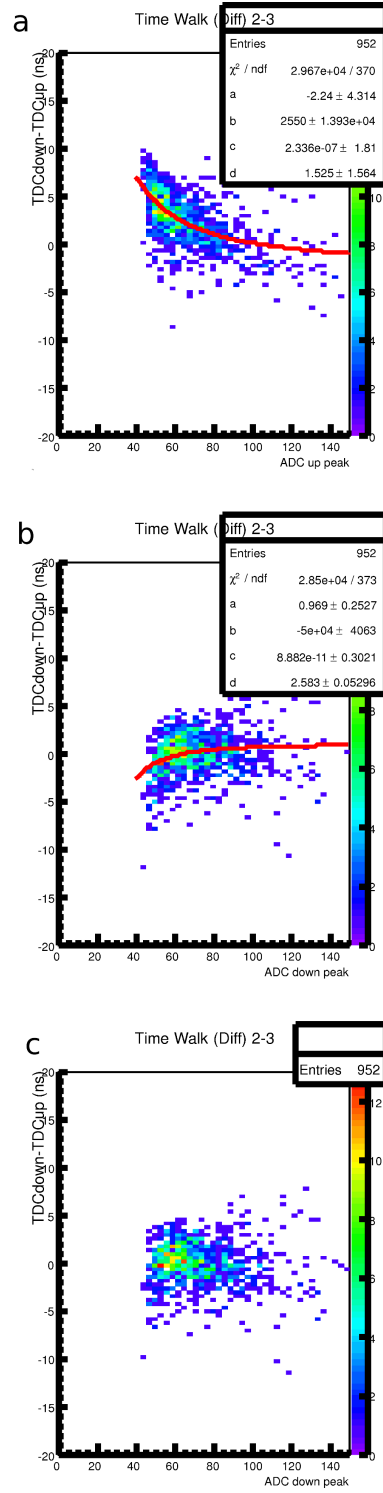


Figure 6.12: Time walk correction. a) Uncorrected spectrum showing the fit function required to remove time walk upstream. b) The result of the subtraction of the data minus the curve from panel a with a new fit to remove the dependence of ADC downstream. c) The final time walk corrected plot.

in approximately:

- 5% of events in the single SiPM group
- 40% of events in the second SiPM group
- 85% of events in the third SiPM group
- 0% of events in the fourth SiPM group (no TDC electronics are available for the outermost layer)

With only a limited number of events providing TDC information it is not possible to accurately determine the position within the module. The TDC threshold will be adjusted before further calibration is conducted on the BCAL, such that the TDC information can be used.

6.4.4 Timing Information - fADC

It fortunately was possible to calculate the timing information of each pulse based on the shape of the energy distribution (which were all consistent within minor variations) recorded by the fADC, by applying the equations

$$a_L = \frac{S_+ - S_-}{T} \quad (6.3)$$

$$b_L = S_+ - a_L T_+ \quad (6.4)$$

$$t_o = \frac{S_p/2 - b_L}{a_L} \quad (6.5)$$

on the leading edge of each pulse the timing information is extracted [53]. In these equations S_+ represents a point greater than half the pulse height, S_- represents a

point less than half the pulse height, T is the time per bin (4 ns for the fADCs used), S_p is the pulse height, and t_o is the time. A sample of this method is shown in Figure 6.13. The benefit of this technique is that the timing information has very little dependence on the peak height as can be seen in Figure 6.14. However, this method does not center the timing distribution on zero as the time walk correction does, as seen in Figure 6.15. This shift can be accounted for by subtracting the mean of each readout cell for a module from the timing difference to determine the location within the module that the particle traveled through.

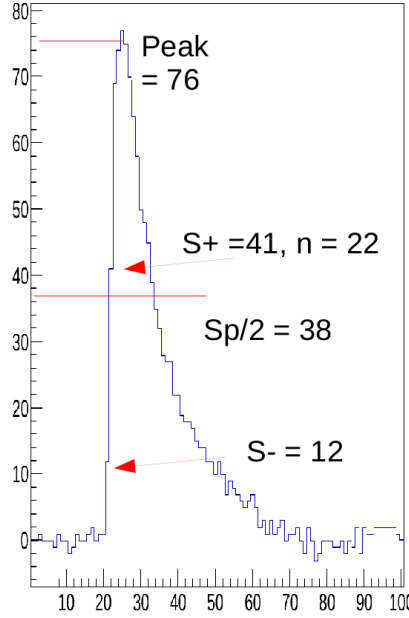


Figure 6.13: Determining the time information through the energy distribution. In this example $a_L=7.25$, $b_L=-597$, and $t_o=87.6$ ns.

6.4.5 Sloped Tracks

With this fADC timing method we were able to have a total of four coordinate points which were used to track the particle's trajectory through the module. The horizontal components were all determined from the timing differences multiplied by the

speed of light in the module, 17.04 cm/ns [54]. The vertical components were determined from the geometrical midpoint of each of the four binning sections, 21.17 cm, 18.08 cm, 12.93 cm, and 4.92 cm for position 1, 2, 3, and 4 respectively, working down from the top of the module. A sample path is shown in Figure 6.16 where the line represents the expected path taken by the particle. This path length was calculated using the method of least squares to determine the slope and intercept. This was done for each event through the module and the resulting angles are presented in a histogram for each column in Figure 6.17.

If the particle traveled along a path L through the module, the energy can be corrected to a vertical path via the equation

$$E' = \frac{E}{\sqrt{1 + (1/L^2)}} \quad (6.6)$$

where E' is the corrected energy, E is the uncorrected energy, and L is the path length through the module.

The uncorrected energy spectrum is shown in Figure 6.18 while the corrected energy spectrum is shown in Figure 6.19. The outer two columns are not shown due to low statistics and fit quality. It is important to note that the tail of the distribution is reduced and the distribution is more Gaussian in shape as expected.

6.5 Results

After each module was analyzed, the mean and sigma of the energy deposition was extracted for each cell such that they could be compared to the other modules. The results of the upstream energy deposition are shown in Figure 6.20 where the two outer columns are not shown. This is because of low statistics collected on the end

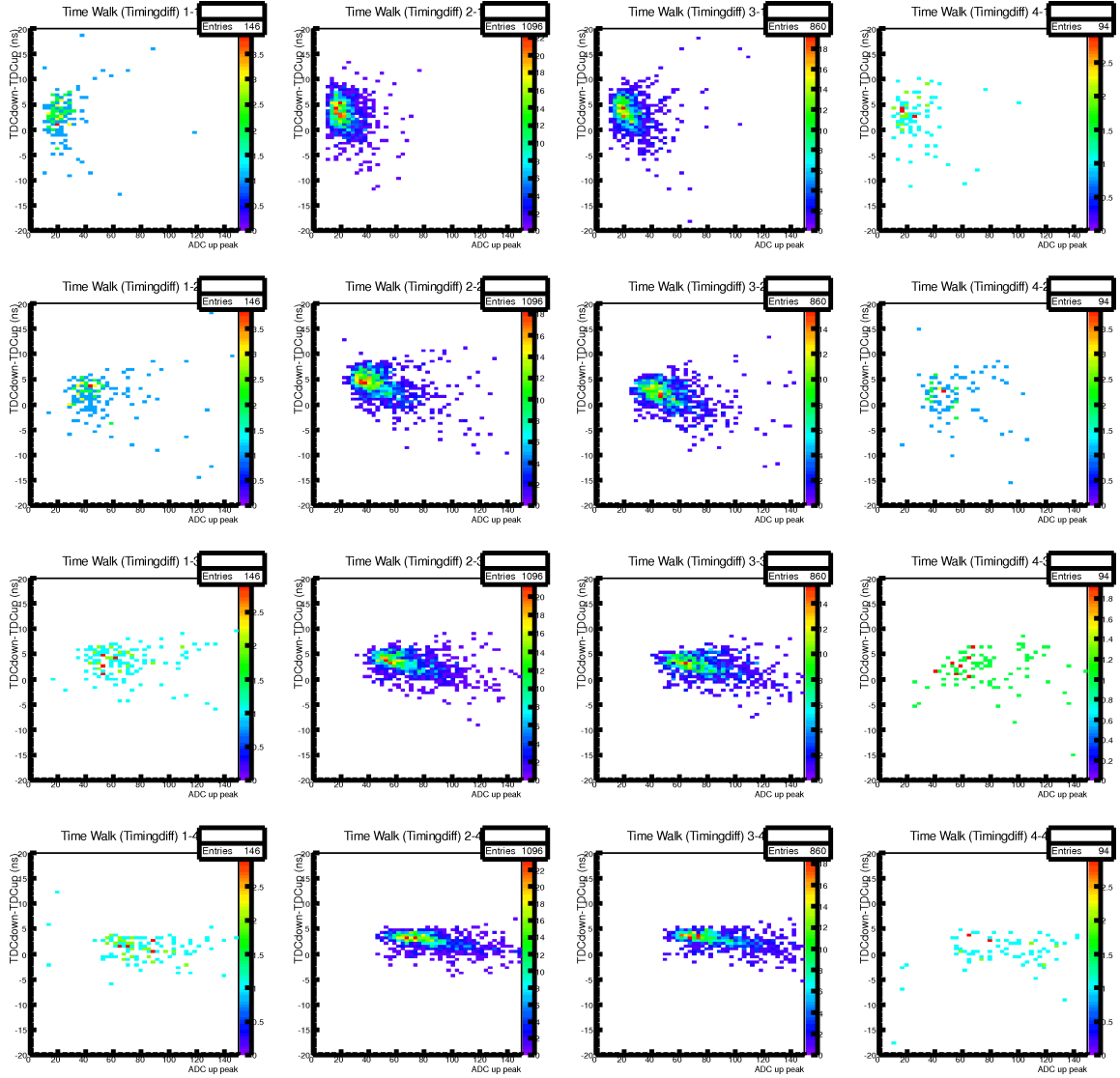


Figure 6.14: Timing difference from the fADC versus maximum peak height as a scatter plot. The uniform distribution of the plot shows that there is no correlation between the energy of the pulse and the timing difference.

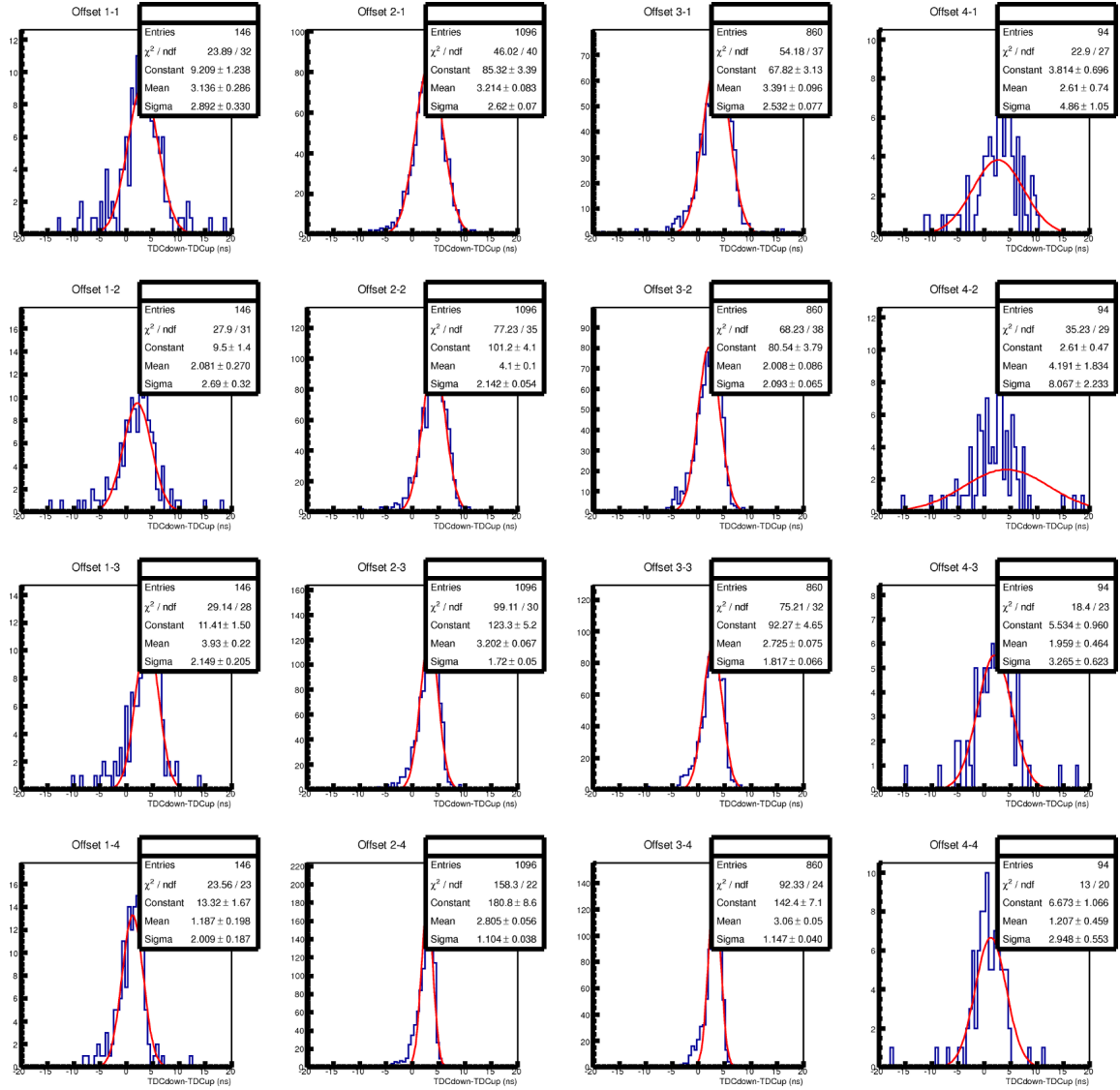


Figure 6.15: Timing difference from the fADC versus maximum peak height as a histogram. Note that the outer two columns have wider distributions owing in large part to the low amount of statistics gathered.

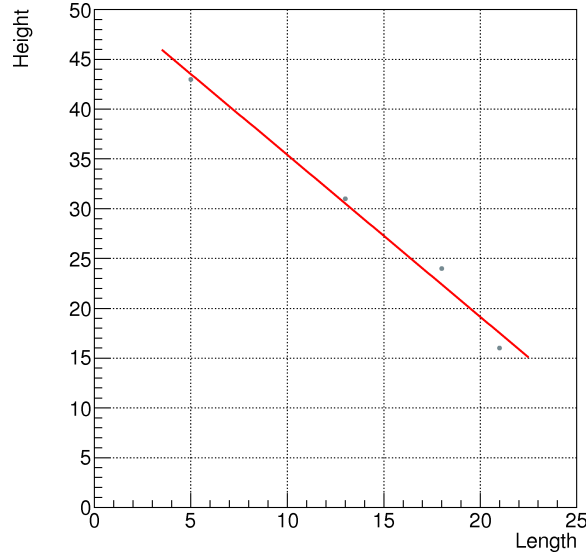


Figure 6.16: Example track through a module where the x-axis is the height component and the y-axis the the length component. This is done in a manner that vertical tracks have a slope of 0 and not infinity.

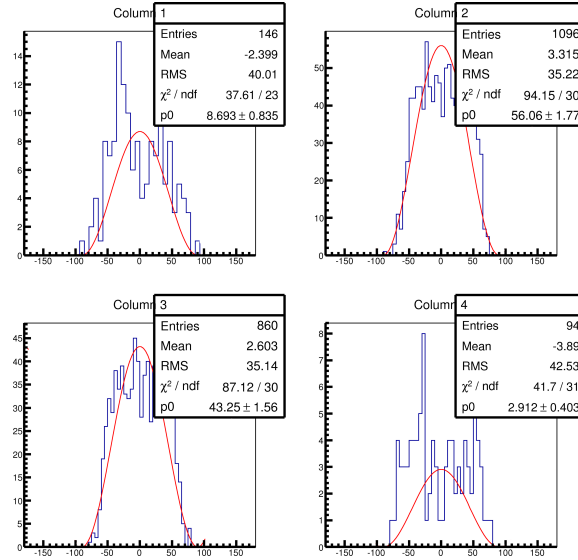


Figure 6.17: The angle of each event through a specific column in the module. Each histogram is fit with a $\cos^2\theta$, the expected cosmic angular deposition. The first and fourth columns have poor fits due to the low statistics collected. The non-zero means indicate that the trigger counter was not centered perfectly under the module.

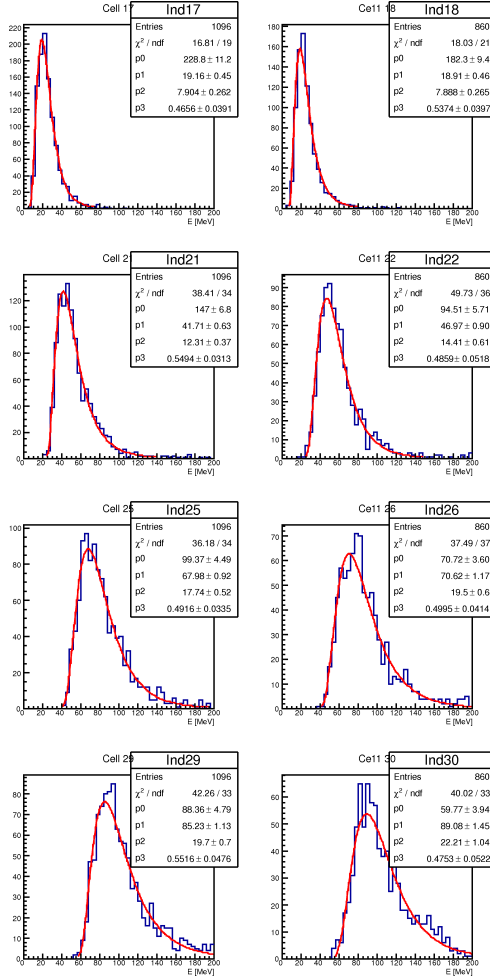


Figure 6.18: Uncorrected energy distribution for the two middle columns of a single module.

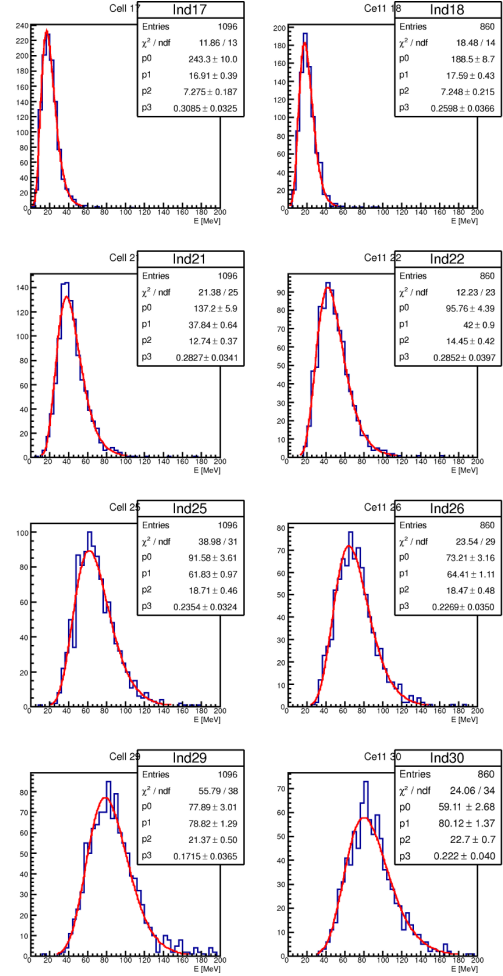


Figure 6.19: Corrected energy distribution for the same module seen in Figure 6.18.

columns due to the trigger scintillator being too narrow to cover the entire width of the module. The sides of the modules also contain damaged and broken fibres that were cut during the machining process to form the wedge. These fibres will lose a part or all of the light collected which will alter the energy deposition in those cells.

The first row has the tightest grouping of energy deposition while the fourth row has the largest spread. This is unsurprising given that the summing effects in the lower layers are more pronounced with every added SiPM as the individual contributors to each sum were not gain matched to each other. With so few data points it is also difficult to determine if an outlier is significant to the overall data trend or was simply different than expected.

The average of column two and three was used to compare to the expected values for energy deposition and shown in Table 6.2. While the energy is lower than expected for every column, it is possible that the expected energy overestimates the amount of light expected to reach the SiPMs likely by overestimating the fibre volume fraction. In the future this may be modeled via Monte Carlo simulations to determine a more accurate expected energy value.

Table 6.2: The average energy deposition for the two middle columns of the modules as well as the expected values, together with the percent detected (mean/expected energy)

Averaged Energy Deposition (MeV)	Expected (MeV)	Percentage (%)
17 ± 7	22	76
37 ± 13	45	82
55 ± 18	69	80
69 ± 22	109	63

An important quantity to know for the BCAL is the ratio of energy depositions between the upstream and downstream sides because it tells us where in the module a particle interacted by the attenuation of the signal that occurred to either end.

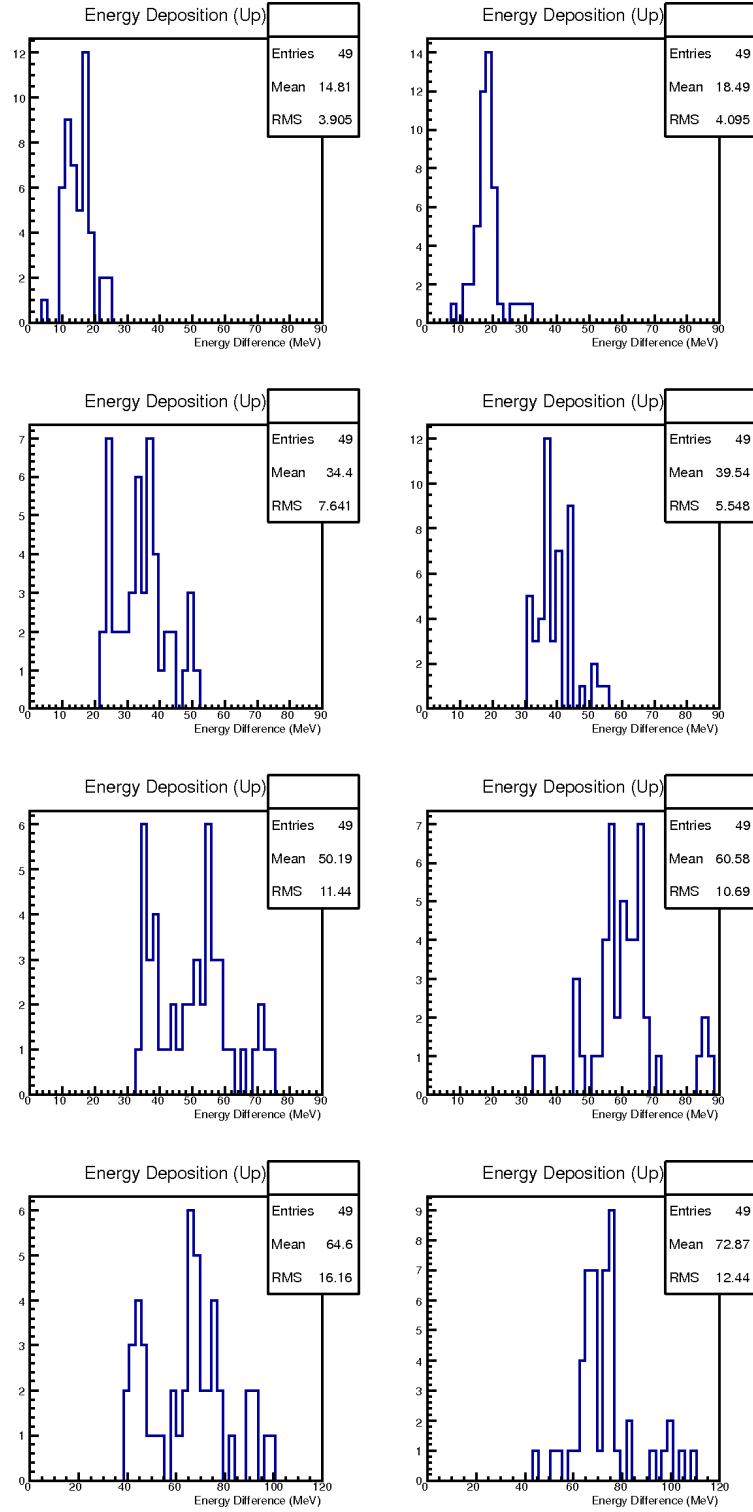


Figure 6.20: The energy deposition for each upstream cell of all the modules. Each entry represents the energy deposition of a single module for that particular cell. If multiple tests had been conducted on a module the results were combined into a single entry.

Given the approximate centering of the trigger counter under the module, as well as the inclusion of the slope corrections, we expect an up/down ratio of approximately 1. This analysis is conducted for each module individually as shown in Figure 6.21 where the energy deposition for each event is used. The means of each of those histograms is shown in Figure 6.22, with each entry representing one module. Only the middle two columns are shown, for the reasons explained previously. The results of Figure 6.22 are averaged for the two columns and tabulated in Table 6.3, where each cell is, as expected, close to one with a sigma of approximately 0.15. This indicates that there is good agreement between the upstream readout assembly and the downstream readout assembly. The spread in data is due to only the rough gain matching that had been done by setting the bias of the SiPMs to the recommended values by the manufacturer. Future calibrations must be done that more accurately match the gains to each other.

The last manner in which the energy deposition is analyzed is to compare the ratio of cells in a single row as shown in Figure 6.23 for all the modules. The results of Figure 6.23 are averaged for columns two and three and presented in Table 6.4 as well as the expected ratios. It can be seen that these values agree well with the expected values for each of the ratios. Improved gain matching will likely improve the sigma on these values leading to tighter distributions.

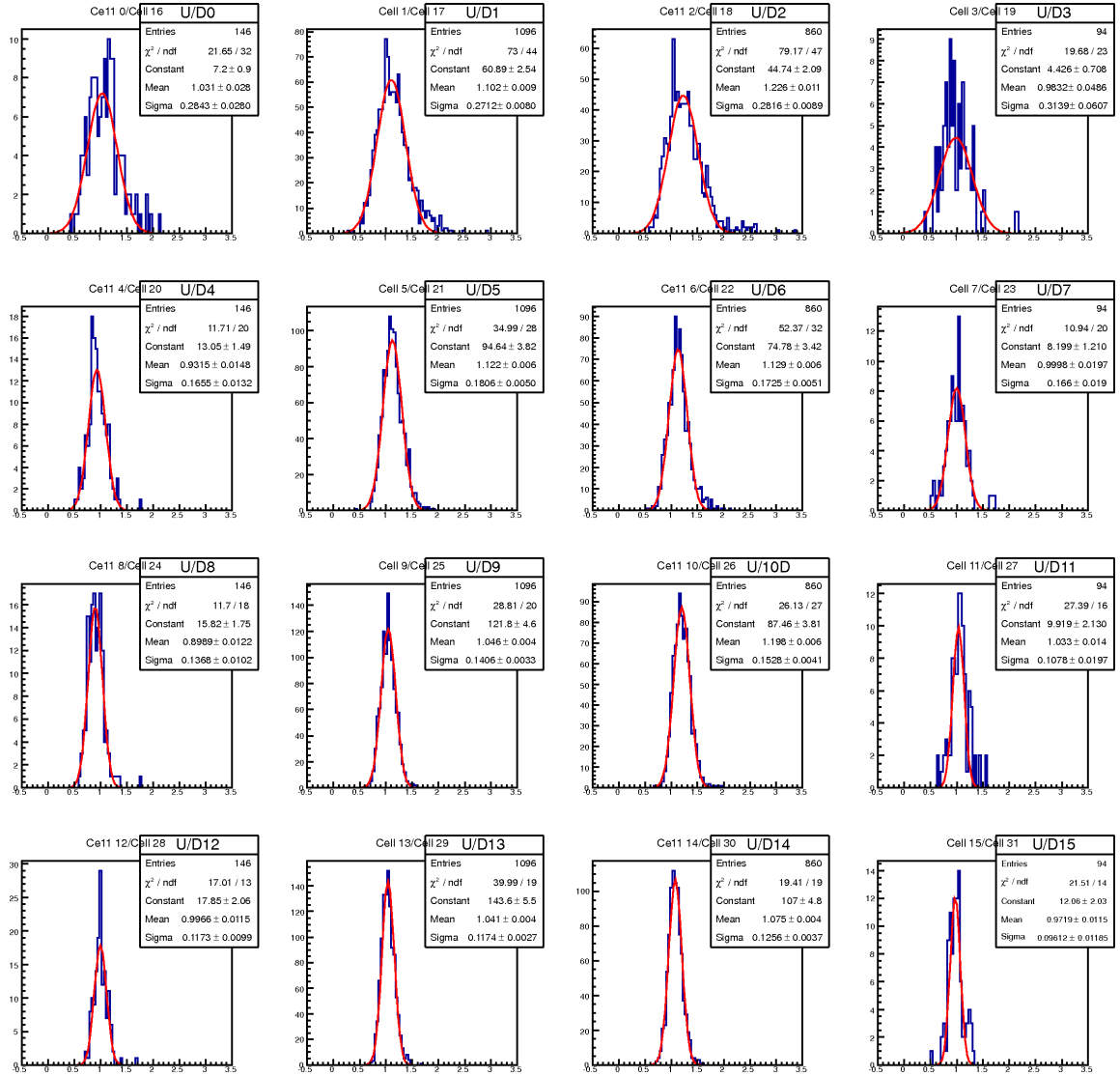


Figure 6.21: The up/down ratio for each cell of a single module.

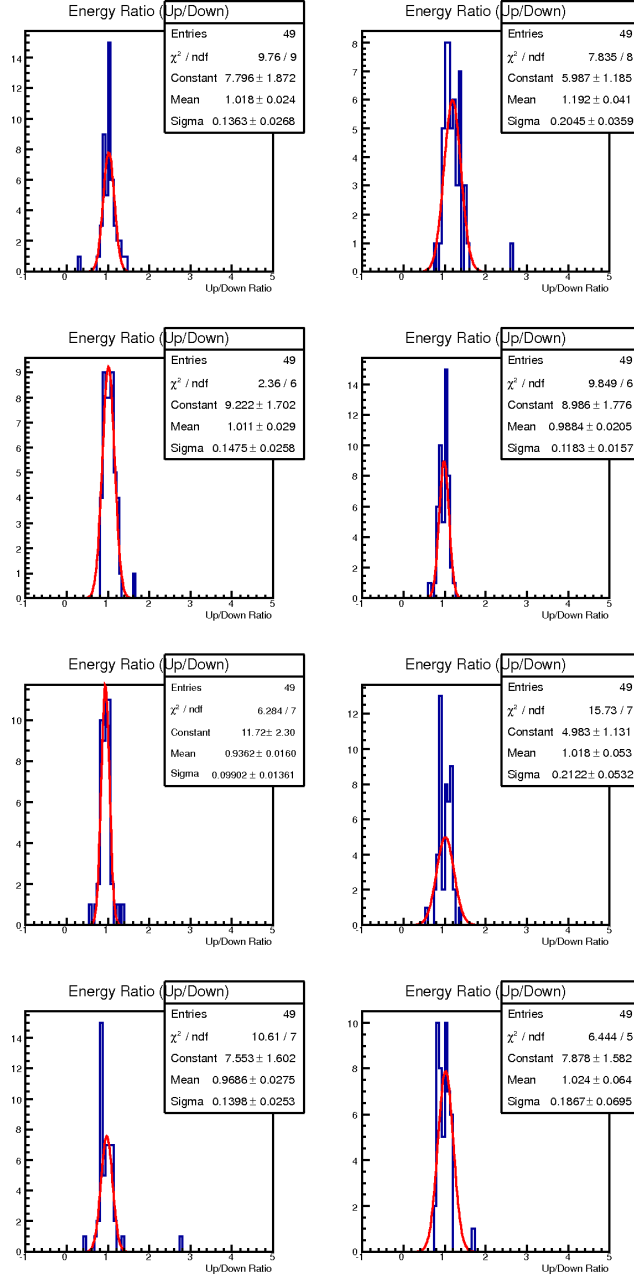


Figure 6.22: The up/down ratios of all modules for the middle 2 columns.

Table 6.3: The various ratios of cells for the two middle columns on the upstream end for all modules.

Row	$\mu \pm \sigma$
1	1.11 ± 0.13
2	1.00 ± 0.11
3	0.98 ± 0.14
4	1.00 ± 0.12

Table 6.4: The various ratios of cells for the two middle columns on the upstream end for all modules.

Cell#/Cell#	Ratio	Expected Ratio
2/1	2.2 ± 0.2	2.0
3/1	3.4 ± 0.2	3.0
4/1	4.0 ± 0.6	4.0
3/2	1.5 ± 0.1	1.5
4/2	1.8 ± 0.1	2.0
4/3	1.21 ± 0.08	1.3

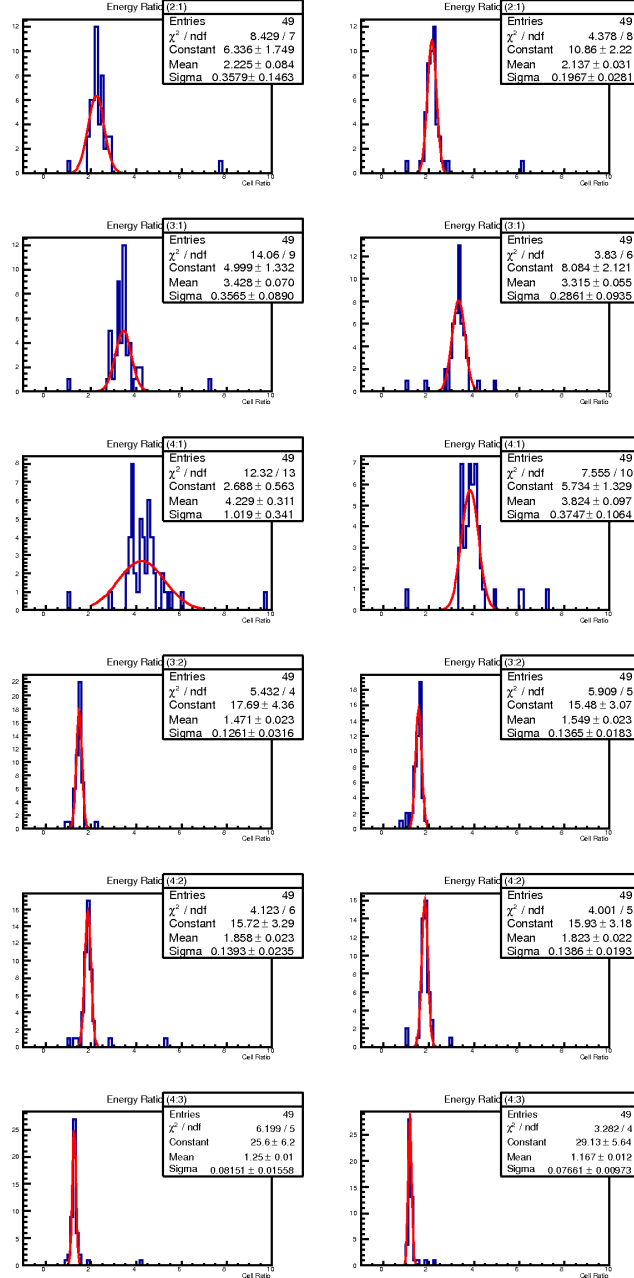


Figure 6.23: The various ratios of cells for the two middle columns on the upstream end for all modules. Note that in the label of each histogram the labeling row i:row j is row i/ row j.

Chapter 7

Conclusions

The GlueX experiment intends to investigate and map out the gluonic degrees of freedom in Quantum Chromodynamics in order to elucidate the phenomenon of quark confinement in pairs and or triplets. In order for this project to succeed, it is necessary that the detector systems are able to provide signals that can be understood and effectively utilized. The final state measurements are critical in determining the intermediate states and the existence of any exotic hybrid mesons.

Many different detectors will be utilized in the GlueX experiment, each needed to measure the four-momenta of the particles of interest. The Barrel Calorimeter was designed to surround the target and provide near 4π coverage in solid angle for photons in the 11° to 126° polar angle range. The BCAL was constructed from 48 modules built from alternating layers of lead sheets and scintillating fibres in order to produce an electromagnetic sampling calorimeter. Each end of the 48 modules will be monitored using 40 light guides and SiPM pairs arranged in a 4 by 10 grid. After attaching each set of light guides onto the module, it was necessary to check the optical interface and ensure good light propagation.

SiPMs were chosen as the readout component of the BCAL detector due to their

compact design and immunity to magnetic fields. However, it is necessary to optimize their supplied voltage to their ideal voltage in order to achieve a uniform gain across the entire BCAL. Effort must be taken to ensure that proper gain matching is done on these SiPMs as even a small fluctuation in the supplied voltage can have a very significant effect on the gain. By maintaining the system at 5°C, the amount of noise will be significantly reduced and the SiPMs can all be calibrated for this operating temperature.

Having checked the response of each module, it was found that they all gave fairly uniform results and agreed in large part to the expected energy deposition of cosmic muons. Given the limitations on the amount of data collected as well as the experimental design only preliminary conclusions can be made. The data tracks with what is expected in terms of up/down ratios and the various ratios between the rows. The energy deposition is found to be lower than is expected which will be investigated by Monte Carlo simulations to form a more rigorous value for the expected energy deposition in each layer. It is important the SiPMs be appropriately gain matched to one another in order to reduce the spread seen in the energy deposition and pulse ratio histograms. In the future, additional calibration tests should be conducted with longer run times in order to allow for greater statistics. Tests should also be conducted with a veto trigger situated above the module to capture only vertical and near vertical events. Lastly, the TDC threshold must be re-calibrated such that the vast majority of events also contain timing information.

Appendix A

Author's Contributions:

- Assisted in determining the resistances of a collection of eight resistors that were used during the construction of the readout assemblies, which will monitor the BCAL. These resistors will be used to help lower the voltage supplied to each SiPM in the readout assembly such that it is more closely matched to its specified voltage supplied by the manufacturer.
- Conducted approximately half the the LED and cosmic tests that were carried out on the modules following the gluing phase to ensure that the light guides were properly installed. This consisted of cabling each module, ensuring sufficient blanket coverage to block out light, and the operation of the electronics and DAQ systems.
- Analyzed the data obtained through cosmic ray tests on each of the modules. This information was used to determine the mean energy deposition in each cell of the readouts for every module as well as how consistent these results were for each module.

Bibliography

- [1] Jefferson Science Associates. JSA News. <http://www.jsallc.org/news/20060412.html>.
- [2] Nathan Isgur and Jack Paton. Flux-Tube Model for Hadrons in QCD. *Phys. Rev. D*, 31(11):2910–2929, Jun 1985.
- [3] David J. Gross. Twenty Five Years of Asymptotic Freedom. *Nuclear Physics Supplements*. 74 (1999) 426-446.
- [4] Robin Devenish and Amanda Cooper-Sarkar. Deep Inelastic Scattering. *Oxford University Press*, 2004.
- [5] David Griffiths. An Introduction to Quantum Field Theory. *Wiley-VCH*, 2011.
- [6] Wikimedia. http://commons.wikimedia.org/wiki/File:Meson_nonet_-_spin_1.svg.
- [7] Michael E. Peskin and Daniel V. Schroeder. Introduction to Elementary Particles. *ABP*, 1997.
- [8] C. Amsler et al. Quark Model. *The Particle Data Group*, 2011. <http://pdg.lbl.gov/2013/reviews/rpp2012-rev-quark-model.pdf>
- [9] V Mathieu et al. The Physics of Glueballs. *arXiv:0810.4453[hep-ph]*

- [10] Wolfgang Ochs. The Status of Glueballs. *Journal of Physics G* 40 (2013) 043001
- [11] Nathan Isgur and Jack Paton. Flux-tube model for hadrons in QCD. *Physical Review D* Volume 31, number 11, June 1985
- [12] Kathryn Janzen. Optimization of Performance Parameters for Large Area Silicon Photonmultipliers for use in the GlueX Experiment. Master's thesis, University of Regina, January 2010.
- [13] Frederick V. Murphy and David E. Yount. The Photon as Hadron. SLAC-PUB-964.
- [14] The GlueX Collaboration. An Initial Study of Mesons and Baryons Containing Strange Quark with GlueX. GlueX-doc-2198-v10.
- [15] Wikipedia Branching Fraction http://en.wikipedia.org/wiki/Branching_fraction
- [16] Klaus Peters. A Primer on Partial Wave Analysis. *Int. J. Mod. Phys. A* 21 (2006) 5618-5624
- [17] Curtis A. Meyer. Physics and Detector Performance Metrics for the GlueX Experiment. Technical report, GlueX Collaboration, 2008. GlueX-doc-1063-v4.
- [18] Kei Moriya. The GlueX Experiment and the Hunt for Exotic States at Jlab. Technical report, GlueX Collaboration, 2011. GlueX-doc-1773-v1.
- [19] Igor Senderovich. A Polarized High-Energy Photon Beam for Production of Exotic Mesons. Technical report, GlueX Collaboration, 2012. GlueX-doc-2096-v1.

- [20] Jim Stewart. The Technical Design of the Hall-D Polarized Photon Beam at the Thomas Jefferson National Accelerator Facility. Technical report, GlueX Collaboration, 2009. GlueX-doc-1127-v4.
- [21] Zisis Papandreou. The GlueX Project at Jefferson Lab - Hadron 07. Technical report, GlueX Collaboration, 2007. GlueX-doc-921-v1.
- [22] Igor Senderovich. Search for Gluonic Excitations in Hadrons with GlueX. Technical report, GlueX Collaboration, 2011. GlueX-doc-1780-v3.
- [23] Richard Wigmans. *Calorimetry: Energy Measurement in Particle Physics*. Oxford Science Publications, 2000.
- [24] Institute of High Energy Physics. KLOE. http://english.ihep.cas.cn/ic/ip/200909/t20090901_35100.html
- [25] Zisis Papandreou. BCAL Calorimetry Response. Technical report, GlueX Collaboration, 2008. GlueX-doc-840-v2.
- [26] Zisis Papandreou et al. Hall D/GlueX Technical Design Report. Technical report, GlueX Collaboration, 2014. GlueX-doc-2442-v1.
- [27] B.D. Leverington et al. Performance of the Prototype Module of the GlueX Electromagnetic Barrel Calorimeter. Technical report, GlueX Collaboration, 2008. GlueX-doc-1071-v3.
- [28] Zisis Papandreou. BCAL Overview For Readout Review. Technical report, GlueX Collaboration, 2009. GlueX-doc-1308-v2.
- [29] Andrei Semenov. Analysis of Amplitude Information from 2006 BCAL Cosmics. Technical report, GlueX Collaboration, 2007. GlueX-doc-845-v4.

- [30] Kuraray. Plastic Scintillating Fibers (Materials and Structures). <http://kuraraypsf.jp/psf/index.html>.
- [31] Elton Smith. BCAL Light Guide Installation and Rework Procedure. Technical report, GlueX Collaboration, 2013. GlueX-doc-2038-v2.
- [32] Elton Smith. Acceptance Studies for the Production Light Guides of the BCAL. Technical report, GlueX Collaboration, 2011. GlueX-doc-1784-v3.
- [33] Adrian C. Melissinos. Experiments in Modern Physics. Academic Press, 2003.
- [34] Hamamatsu. Environmental Resistance and Reliability. http://www.hamamatsu.com/resources/pdf/etd/PMT_handbook_v3aE-Chapter13.pdf
- [35] D. Renker. Geiger-Mode avalanche photodiodes, history, properties, and problems. *Nucl. Instr. Meth.*, A567:48-56, 2006.
- [36] PerkinElmer precisely. Avalanche photodiode: A User Guide. www.optoelectronics.perkinelmer.com
- [37] Solid State Division. Characteristics and use of Si APD(Avalanche Photodiode). <http://hep.ucsb.edu>
- [38] Formation of Depletion Layer in Diode. Characteristics and use of Si APD(Avalanche Photodiode). <http://www.daenotes.com/electronics/devices-circuits/formation-depletion-layer-diode>
- [39] P. Buzhan et al. An Advanced Study of Silicon Photomultiplier. <http://www.slac.stanford.edu/pubs/icfa/fall01/paper3/paper3.pdf>

- [40] Giancarlo Barbarino et al. Silicon Photo Multipliers Detectors Operating in Geiger Regime: an Unlimited Device for Future Applications, Photodiodes - World Activities in 2011 ISBN: 978-953-307-530-3.
- [41] Mehrnoosh Tahani. Large Area Multipixel Photon Counters on the Search for Exotic Hybrid Mesons at GlueX. Master's thesis, University of Regina, July 2012.
- [42] I. Britvitch et al. Investigation of a photon counting avalanche photodiode from Hamamatsu photonics. *Nucl. Instr. Meth.*, A567:276-280, 2006.
- [43] I. Britvitch et al. Investigation of Photon Counting Avalanche Photodiodes from Hamamatsu Photonics <http://ndip.in2p3.fr/beaune05/cdrom/Posters/PI-28-renker.pdf>
- [44] Patrick Hallen. Determination of the Recovery Time of Silicon Photomultipliers. Bachelor's thesis, RWTH Aachen University, September 2011.
- [45] sensl. An Introduction to the Silicon Photomultiplier. <http://www.sensl.com>
- [46] A. Intermite et al. Influence of Dark Count on the Performance of Silicon Photomultipliers. http://www.lanl.gov/conferences/biw10/preprints/TUPSM046_preprint.pdf
- [47] R. Pagano et al. Optimized Silicon Photomultipliers with optical trenches. <http://ieeexplore.ieee.org/stamp/stamp.jsp?arnumber=06044204>
- [48] Adam Para. Characterization of MPPC/SiPM/GMAPDs.
- [49] E.G. Anassontzis et al. Relative gain monitoring of the GlueX calorimeters *Nucl. Instr. Meth.*, A738:41-49, 2014.

- [50] Stamatis Katsaganis. The Electromagnetic Calorimeter of the GlueX Particle Detector. Master's thesis, University of Regina, September 2011
- [51] Hovannes Egiyan. Slow Controls Progress May 2014. Technical report, GlueX Collaboration, 2014. GlueX-doc-2467-v3.
- [52] Blake Leverington. The GlueX Lead-Scintillating Fibre Electromagnetic Calorimeter. PhD thesis, University of Regina, September 2010.
- [53] J. V. Bennett et. al. Precision timing measurement of phototube pulses using a flash analog-to-digital converter.
- [54] Tegan Beattie. Attenuation Length and the Speed of Light in a BCAL Prototype Module Measured Using Pre-production SiPMs and Cosmics. Technical report, GlueX Collaboration, 2012. GlueX-doc-2049-v2.
- [55] David Griffiths. An Introduction to Quantum Field Theory. *Wiley-VCH*, 2011.
- [56] Tara Bogart. Initial Testing of the Barrel Calorimeter Monitoring System of the GlueX Particle Detector. Technical report, GlueX Collaboration, 2012. GlueX-doc-2045-v1.